

15 Stellar Winds

Stan Owocki

Bartol Research Institute, Department of Physics and Astronomy,
University of Colorado, Newark, DE, USA

1	<i>Introduction and Background</i>	737
2	<i>Observational Diagnostics and Inferred Properties</i>	740
2.1	Solar Corona and Wind	740
2.2	Spectral Signatures of Dense Winds from Hot and Cool Stars	742
2.2.1	Opacity and Optical Depth	742
2.2.2	Doppler-Shifted Line Absorption	744
2.2.3	Asymmetric P-Cygni Profiles from Scattering Lines	745
2.2.4	Wind-Emission Lines	748
2.2.5	Continuum Emission in Radio and Infrared	750
3	<i>General Equations and Formalism for Stellar Wind Mass Loss</i>	751
3.1	Hydrostatic Equilibrium in the Atmospheric Base of Any Wind	751
3.2	General Flow Conservation Equations	752
3.3	Steady, Spherically Symmetric Wind Expansion	753
3.4	Energy Requirements of a Spherical Wind Outflow	753
4	<i>Coronal Expansion and Solar Wind</i>	754
4.1	Reasons for Hot, Extended Corona	754
4.1.1	Thermal Runaway from Density and Temperature Decline of Line-Cooling	754
4.1.2	Coronal Heating with a Conductive Thermostat	756
4.1.3	Incompatibility of Hot Extended Hydrostatic Corona with ISM Pressure	756
4.2	Isothermal Solar Wind Model	757
4.2.1	Temperature Sensitivity of Mass Loss Rate	759
4.2.2	The Solar Wind as a Thermostat for Coronal Heating	760
4.3	Driving High-Speed Streams	761
4.4	Relation to Winds from other Cool Stars	761
4.4.1	Coronal Winds of Cool Main-Sequence Stars	761
4.4.2	Alfvén Wave Pressure Driving of Cool-Giant Winds	762
4.4.3	Superwind Mass Loss from Asymptotic Giant Branch Stars	763
4.5	Summary for the Solar Wind	764
5	<i>Radiatively Driven Winds from Hot, Massive Stars</i>	765
5.1	Radiative Acceleration	765
5.1.1	Electron Scattering and the Eddington Limit	765
5.1.2	Driving By Doppler-Shifted Resonant Line Scattering	766
5.1.3	Radiative Acceleration from a Single, Isolated Line	767

5.1.4	Sobolev Localization of Line-Force Integrals for a Point Star	767
5.2	The CAK Model for Line-Driven Winds	768
5.2.1	The CAK Line-Ensemble Force	768
5.2.2	CAK Dynamical Solution for Mass Loss Rate and Terminal Speed	769
5.3	Extensions of Idealized CAK Model	771
5.3.1	Finite-Size Star	771
5.3.2	Radial Variations in Ionization	771
5.3.3	Finite Gas Pressure and Sound Speed	772
5.4	Wind Instability and Variability	772
5.5	Effect of Rotation	774
5.6	Summary for Radiatively Driven Massive-Star Winds	776
6	<i>Wolf-Rayet Winds and Multiline Scattering</i>	778
6.1	Example of Multiple Momentum Deposition in a Static Gray Envelope	778
6.2	Multiline Transfer in an Expanding Wind	780
6.3	Wind Momentum–Luminosity Relation for WR Stars	781
6.4	Cumulative Comoving-Frame Redshift from Multiline Scattering	782
6.5	Role of Line Bunches, Gaps, and Core Thermalization	783
6.6	Summary for Wolf-Rayet Winds	785
	<i>References</i>	786

Abstract: A “stellar wind” is the continuous, supersonic outflow of matter from the surface layers of a star. Our sun has a solar wind, driven by the gas-pressure expansion of the hot ($T > 10^6$ K) solar corona. It can be studied through direct *in situ* measurement by interplanetary spacecraft; but analogous coronal winds in more distant solar-type stars are so tenuous and transparent that they are difficult to detect directly. Many more luminous stars have winds that are dense enough to be opaque at certain wavelengths of the star’s radiation, making it possible to study their wind outflows remotely through careful interpretation of the observed stellar spectra. Red giant stars show slow, dense winds that may be driven by the pressure from magnetohydrodynamic waves. As stars with initial mass up to $8 M_{\odot}$ evolve toward the Asymptotic Giant Branch (AGB), a combination of stellar pulsations and radiative scattering off dust can culminate in “superwinds” that strip away the entire stellar envelope, leaving behind a hot white dwarf stellar core with less than the Chandrasekhar mass of $\sim 1.4 M_{\odot}$. The winds of hot, luminous, massive stars are driven by *line-scattering* of stellar radiation, but such massive stars can also exhibit superwind episodes, either as Red Supergiants or Luminous Blue Variable stars. The combined wind and superwind mass loss can strip the star’s hydrogen envelope, leaving behind a Wolf-Rayet star composed of the products of earlier nuclear burning via the CNO cycle. In addition to such direct effects on a star’s own evolution, stellar winds can be a substantial source of mass, momentum, and energy to the interstellar medium, blowing open large cavities or “bubbles” in this ISM, seeding it with nuclear processed material, and even helping trigger the formation of new stars, and influencing their eventual fate as white dwarves or core-collapse supernovae. This chapter reviews the properties of such stellar winds, with an emphasis on the various dynamical driving processes and what they imply for key wind parameters like the wind flow speed and mass loss rate.

1 Introduction and Background

The Sun and other stars are commonly characterized by the radiation they emit. But one of the great astronomical discoveries of the latter half of the past century was the realization that nearly all stars lose mass through a more or less continuous surface outflow called a “stellar wind.” While it was long apparent that stars could eject material in dramatic outbursts like novae or supernovae, the concept of continuous mass loss in the relatively quiescent phases of a star’s evolution stems in large part from the direct *in situ* detection by interplanetary spacecraft of a high-speed, supersonic outflow from the sun. For this *solar* wind, the overall rate of mass loss is quite modest, roughly $10^{-14} M_{\odot}/\text{yr}$, which, even if maintained over the sun’s entire main sequence lifetime of ca. 10^{10} year, would imply a cumulative loss of only a quite negligible 0.01% of its initial mass. By contrast, other stars – and indeed even the sun in its later evolutionary stages as a cool giant – can have winds that over time substantially reduce the star’s mass, with important consequences for its evolution and ultimate fate (de Koter et al. 2008; Maeder and Meynet 2000; Leer et al. 1982; Vink 2008; Willson 2008). Moreover, the associated input of mass, momentum, and energy into the interstellar medium can have significant consequences, forming visually striking nebulae and windblown “bubbles” (Castor et al. 1975), and even playing a feedback role in bursts of new star formation that can influence the overall structure and evolution of the parent galaxy (Oey and Clark 2007). In recent years, the general concept of a continuous “wind” has even been extended to describe outflows with a diverse

range of conditions and scales, ranging from stellar accretion disks (Calvet 2004), to Active Galactic Nuclei (Proga 2007), to even whole galaxies (Breitschwerdt and Komossa 2000).

In the half-century since this concept of a wind from the sun or stars took hold, there has amassed a vast literature – consisting of thousands of journal papers, roughly a hundred conference proceedings, dozens of review articles, and even a handful of books – on various aspects of solar and stellar wind mass loss. It is neither feasible nor desirable to attempt any comprehensive survey of this literature, and interested readers looking for entry points beyond the topical coverage here are encouraged to begin with a few key complementary reviews and books. For the solar wind, the original monograph *Interplanetary Dynamics* by Parker (1963) provides a still relevant and fundamental basis, while the recent *Basics of the Solar Wind* by Meyer-Vernet (2007) gives an accessible modern summary. Particularly insightful reviews include those by Leer et al. (1982), Parker (1991), and Cranmer (2009). Proceedings of the regular series of dedicated solar wind conferences, the most recent being *Solar Wind 12* (Maksimovic et al. 2010), also make a good entry point into the evolving solar wind literature. For stellar winds, the text by Lamers and Cassinelli (1999) provides a good general introduction, while more targeted reviews tend to split between those focused on hot, massive stars (Owocki 2001, 2004; Puls et al. 2008) vs. cool, low-mass giants (Holzer and MacGregor 1985; Holzer 1987; Willson 2000; Dupree 2004).

This chapter aims to give a broad physical overview of the properties and processes involved in solar and stellar wind mass loss. A general theme is to identify the *forces* and *energies* that can overcome the gravitational binding that holds material onto a nearly hydrostatic stellar surface, and thereby lift and accelerate the outermost layers into a sustained outflow through which material ultimately escapes entirely the star’s gravitational potential. This competition between outward driving and inward gravity is key to determining two basic wind characteristics, namely the mass loss rate \dot{M} and terminal flow speed v_∞ .

Stellar wind mass loss rates span many decades, reaching more than a billion times that of the solar wind, $\dot{M} > 10^{-5} M_\odot/\text{yr}$, for luminous giant stars; the exact values depend crucially on the specific wind driving mechanism. But for a wide range of driving mechanisms, a quite general rule of thumb is that the wind terminal speed v_∞ scales in proportion to the escape speed v_e from the stellar surface. One intuitive way to think of the process is that in general the outward driving mechanism tends to tune itself to siphon off just enough mass from the star to keep the outward force an order-unity factor above gravity; the net effective “antigravity” means wind material effectively “falls off” the star, reaching a final speed comparable to v_e .

In practice, the proportionality factor can vary from about a third (for red giants) to about factor three (for blue supergiants). Note that in the former case 90% of the energy to drive the wind is expended in lifting the material out of the star’s gravitational potential, with the remaining 10% expended in acceleration to the terminal flow speed; in the latter case, this relative allotment of energy is reversed. The total wind energy loss rate, $L_{\text{wind}} \equiv \dot{M}(v_e^2 + v_\infty^2)/2$, is typically only a tiny fraction of the star’s radiative luminosity, about 10^{-6} for the solar wind, and ranging up to a few percent for winds from luminous, massive stars. During brief “superwind” episodes of massive “Luminous Blue Variable” (LBV) stars, the radiative and wind luminosity can even become comparable.

The specific driving mechanisms vary with the various types of stellar wind, which can be broadly organized into three general classes:

1. *Coronal Winds* from the Sun and Other Cool, Main-Sequence Stars. These can be characterized as thermally or *gas pressure driven*, with the main outward force to overcome gravity stemming from the gas-pressure gradient associated with the high-temperature corona. The

key issues thus lie in understanding how mechanical energy generated in the near-surface convection zone is transmitted upward (e.g., via wave oscillations in the magnetic field) to heat and drive a high-temperature coronal expansion. While important as a prototype, and because the earth itself is embedded in the solar coronal wind, the low \dot{M} means such coronal winds have negligible direct effect on the star's evolution. (On the other hand, the loss of angular momentum in magnetized coronal winds does seem sufficient to cause an evolutionary decline of rotation rates in the sun and other cool stars; Weber and Davis 1967; Scholz 2009).

2. *Winds from Cool Giants and Supergiants.* The lower surface gravity of giant stars facilitates much stronger, but slower wind mass loss. For example, the slow ($v_\infty \sim 10\text{--}50$ km/s), moderately strong ($\dot{M} \sim 10^{-8} M_\odot/\text{yr}$) winds of Red Giants may be driven by the direct momentum (vs. energy) addition of magnetic Alfvén waves. But in later evolutionary stages, stellar pulsations, perhaps augmented by radiative *scattering* on dust, can apparently induce a much stronger, even runaway mass loss. Over the final few thousand years, this can reduce stars with initial mass as high as $8 M_\odot$ to a remnant white dwarf below the Chandrasekhar limit of $\sim 1.4 M_\odot$! Similarly, initially hot stars with $M \approx 8\text{--}40 M_\odot$ can evolve through a Red Supergiant phase, with a strong mass loss that has important consequences for their subsequent evolution and eventual demise as core-collapse supernovae (SN).
3. *Winds from Hot, Massive, Luminous Stars.* The high luminosity of hot, massive stars means that the momentum of the light scattering off the electrons and ions in the atmosphere is by itself able to overcome the gravity and drive winds with $v_\infty \sim (1\text{--}3)v_e \sim 1,000\text{--}3,000$ km/s and $\dot{M} \sim 10^{-10}\text{--}10^{-5} M_\odot/\text{yr}$. As quantified in the so-called CAK (after Castor et al. 1975) formalism, for winds from OB-type stars the essential coupling between radiative momentum and gas is via *line scattering* by heavy, minor ions; regulation of the driving by line saturation leads to relatively simple, analytic scaling laws for the dependence of mass loss rate and flow speed on stellar parameters like luminosity, mass, and radius. In the subclass known as Wolf-Rayet (WR) stars, the mass loss is so high that the stellar “photosphere” lies in the wind itself, characterized now by strong wind-broadened emission lines of helium and abundant heavy elements like carbon, nitrogen, or oxygen (CNO); in evolved WR stars the depletion or absence of hydrogen indicates the mass loss has actually stripped away the star's original hydrogen envelope, exposing a core of material processed by various stages of nuclear burning. This mass loss may also be augmented by Luminous Blue Variable (LBV) phases characterized by eruptions or “superwinds” with mass loss rates up to $0.01\text{--}1 M_\odot/\text{yr}$ lasting several years or decades. The 1840-60 giant eruption of η Carinae provides a key prototype.

Of these, the first and third have the more extensively developed theory, and as such will constitute the major focus of detailed discussion below. For the second class, the reader is referred to previous reviews (Holzer and MacGregor 1985; Holzer 1987; Willson 2000; Dupree 2004) and references therein. (See, however, [▶ Sect. 4.4](#) below.)

The next section ([▶ Sect. 2](#)) summarizes the diagnostic methods and resulting inferred general properties for these various classes of stellar wind. The following section ([▶ Sect. 3](#)) introduces the basic dynamical conservation equations governing wind outflow, which are then applied ([▶ Sect. 4](#)) to the gas-pressure-driven solar wind. The last two sections give a quite extensive discussion of radiatively driven mass loss from hot, massive, luminous stars, including the CAK line-driving of OB winds ([▶ Sect. 5](#)), and the multiline-scattered winds of Wolf-Rayet stars ([▶ Sect. 6](#)).

2 Observational Diagnostics and Inferred Properties

2.1 Solar Corona and Wind

The close proximity of the sun makes it possible to obtain high-resolution observations of the complex magnetic structure in the solar atmosphere and corona, while also flying interplanetary spacecraft to measure in situ the detailed plasma and magnetic field properties of the resulting solar wind. Even before the spacecraft era, early visual evidence that the sun has an outflowing wind came from antisolar deflection of comet tails (Biermann 1951; ▶ [Fig. 15-1a](#)), and from the radial striations seen in eclipse photographs of the solar corona (Newkirk 1967; ▶ [Fig. 15-1b](#)). Nowadays, modern *coronagraphs* use an occulting disk to artificially eclipse the bright solar surface, allowing ground- and space-based telescopes to make routine observations of the solar corona.

▶ [Figure 15-2a](#) (from McComas et al. 1998) combines such coronagraphic images of the inner and outer corona (taken respectively from the SOHO spacecraft, and from the solar observatory on Mauna Loa, Hawaii) with an extreme ultraviolet image of the solar disk (also from SOHO), and a polar line plot of the latitudinal variation of solar wind speed (as measured by the *Ulysses* spacecraft during its initial polar orbit of the sun). The equatorial concentration of coronal brightness stems from confinement of coronal plasma by closed loops of magnetic field, with the outer loops pulled into the radial “helmet” streamers by the outflow of the solar wind. By contrast, the open nature of magnetic field lines over the poles allow material to flow freely outward, making for reduced density *coronal holes* (Zirker 1977). A key point from ▶ [Fig. 15-2a](#) is that the solar wind arising from these polar coronal holes is much steadier and faster (about 750 km/s) than the equatorial, streamer-belt wind measured near the ecliptic (with speeds from



■ Fig. 15-1

Two telescopic clues to the existence of the solar wind. *Left*: The dual tails of Comet Hale–Bopp. The upper one here consists mostly of *dust* slowly driven away from the comet by solar radiation; it is tilted from the antisun (radial) direction by the comet’s own orbital motion. The lower *plasma* tail comes from cometary ions picked up by the solar wind; its more radial orientation implies that the radial outflow of the solar wind must be substantially faster than the comet’s orbital speed. *Right*: White-light photograph of 1980 solar eclipse, showing how the million-degree solar corona is structured by the solar magnetic field. The closed magnetic loops that trap gas in the inner corona become tapered into pointed “helmet” streamers by the outward expansion of the solar wind. Eclipse image courtesy Rhodes College, Memphis, Tennessee, and High Altitude Observatory (HAO), University Corporation for Atmospheric Research (UCAR), Boulder, Colorado. UCAR is sponsored by the National Science Foundation

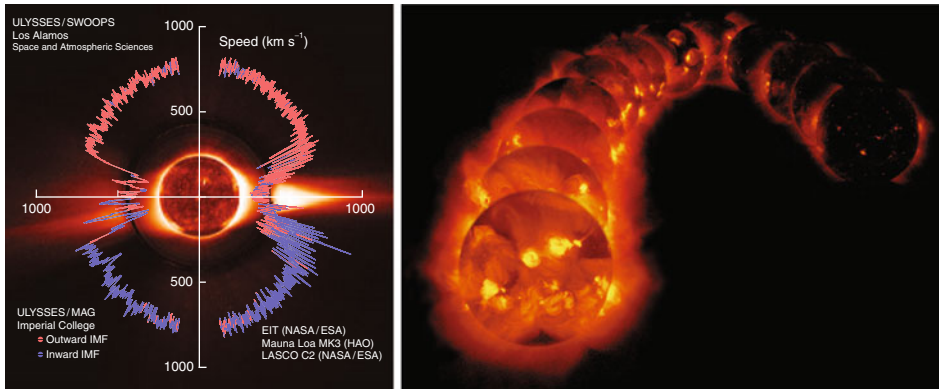


Fig. 15-2

Left: Polar plot of the latitudinal variation of solar wind speed (*jagged lines*) and magnetic polarity (indicated by *red vs. blue* line color), as measured by the *Ulysses* spacecraft during its initial polar orbit of the sun. This is overlaid on a composite of coronagraphic images of the inner and outer corona, and an extreme ultraviolet image of the solar disk, all made on August 17, 1996, near the minimum of the solar sunspot cycle. **Right:** X-ray images of the sun made by the *Yokohoh* satellite from the 1991 solar maximum (*left foreground*) to the 1996 solar minimum (*right background*)

400 to 750 km/s). This provides a vivid illustration of how the magnetic structure of the corona can have a profound influence on the resulting solar wind.

Early direct evidence for the very high coronal temperature came from eclipse observations of emission lines from highly stripped ions of calcium and iron, the most prominent being the Fe^{+13} “green” line at 5,303Å. This stripping of 13 electrons from iron arises from high-energy collisions with free electrons, implying a characteristic electron temperature around one and half million Kelvin (1.5 MK) in the dense, coronal loops that dominate the line emission. Nowadays the high temperature of these coronal loops is most vividly illustrated by soft X-ray images, such as those shown in ▶ [Fig. 15-2b](#) from the observations by the *Yokohoh* satellite made over the 1991–1996 declining phase of the sun’s 11-year magnetic activity cycle. Unfortunately, the relative darkness of coronal holes means it is much more difficult to use emission lines and X-rays to infer the temperature or other properties of these important source regions of the solar wind.

Complementary studies with space-borne coronal spectrographs (such as the UVCS instrument on SOHO; Kohl et al. 1995) use the strength and width of ultraviolet *scattering* lines to infer the flow speed and kinetic temperatures of various ion species throughout the corona. Results show the outflow speed in coronal holes already exceeds 100 km/s within a solar radius from the surface; moreover, ion temperatures are even *higher* than for electrons, up to 4 MK for protons, and 100 MK for oxygen! The recent, very comprehensive review of coronal holes by Cranmer (2009) provides an extensive discussion of how these different temperatures may be linked to the detailed mechanisms for heating the corona, e.g., by magnetic waves excited by the complex convective motions of the solar atmosphere.

In situ measurements by *Ulysses* and many other interplanetary spacecraft show that the solar wind mass flux (given by $\rho v r^2$, the product of density, flow speed, and the square of the local heliocentric radius) is remarkably constant, varying less than a factor two in space and time

(Withbroe 1989). If extended over the full sphere around the sun, the corresponding global mass loss rate works out to $\dot{M} \approx 2 - 3 \times 10^{-14} M_{\odot}/\text{year}$. In the ecliptic plane, the typical flow speed is $v_{\infty} \approx 400 \text{ km/s}$, but it extends up to $v_{\infty} \approx 750 \text{ km/s}$ in both ecliptic and polar high-speed streams that are thought to originate from coronal holes.

Finally, while many other cool, solar-type stars show clear signatures of magnetic activity and hot, X-ray emitting coronae, any associated coronal type winds are simply too tenuous and transparent to be detected directly by any absorption signatures in the spatially unresolved stellar flux. In a handful of stars, there is evidence for an “astrosphere” (Wood 2004), the stellar analog of the bullet-shaped heliospheric cavity carved out by the solar wind as the sun moves through the local interstellar medium. A wall of neutral hydrogen that forms around the nose of this bullet can lead to a detectable hydrogen line absorption in the observed spectrum of stars positioned so that their light passes through this wall on its way to earth. But apart from such indirect evidence, most of what is inferred about coronal winds from other stars is based on analogy or extrapolation of conditions from the much more detailed measurements of the sun’s coronal wind.

2.2 Spectral Signatures of Dense Winds from Hot and Cool Stars

2.2.1 Opacity and Optical Depth

The much higher mass loss rates in stellar winds from both hot and cool giants make them dense enough to become opaque in certain spectral bands, imparting detectable observational signatures in the star’s flux spectrum that can be used to infer key wind conditions. The coupling of wind material to stellar light can take various forms (Mihalas 1978), including:

- Free-electron (Thomson) scattering
- Free-free absorption and emission by electrons near ions
- Bound-free (ionization) absorption and free-bound (recombination) emission by atoms or molecules
- Bound-bound (line) scattering, absorption, and/or emission by atoms or molecules
- Scattering, absorption, and emission by dust grains

In parsing this list, it is helpful to focus on some key distinctions. *Scattering* involves a change in direction of light without true absorption of its energy, while *emission* creates new light, e.g., from the energy within the gas. *Bound-bound* processes lead to narrow wavelength features in the spectrum, known as (absorption or emission) lines. Most other processes involve the broad spectral *continuum* of stellar radiation, albeit with bound-free or free-bound *edges* at the wavelength associated with the energies for ionization/recombination of the ion, or broad variations due to wavelength dependence of the cross section, e.g., for dust.

In the context of determining stellar wind mass loss rates, a particularly key distinction lies between *single-body* processes (e.g., electron scattering, bound-free absorption, or dust scattering and absorption), and *two-body* processes involving both an ion and a free electron (e.g., free-free absorption, and free-free or free-bound emission). The strength of the former scales in proportion to the single density of the species involved, whereas the latter depend on the product of the electron and ion density, and so have an overall *density-squared* dependence. In a wind with a high degree of spatial clumping, such density-squared processes will be enhanced over what would occur in a smooth flow by a clumping factor $C_f \equiv \sqrt{\langle \rho^2 \rangle} / \langle \rho \rangle$,

where the square brackets represent volume averaging on a scale large compared to the clump size. For a wind in which material is mostly in clumps filling only a fraction f_v of the total volume, any mass loss rate diagnostic that scales with ρ^2 will tend to *overestimate* the true mass loss rate by about a factor $C_f = 1/\sqrt{f_v}$. Further details can be found in the proceedings of a recent conference on wind clumping (Hamann et al. 2008).

Single-density continuum processes (e.g., electron scattering, bound-free absorption, or dust scattering and absorption) can be characterized by the opacity, κ , which is effectively a cross section per unit mass, with CGS units cm^2/g . The overall effectiveness of continuum absorption or scattering by the wind depends on the associated *optical depth* from some surface radius R to the observer. Along the radial direction r , this is given by the integral of the wind opacity κ times density $\rho(r)$,

$$\tau_* = \int_R^\infty \kappa \rho(r) dr \approx \frac{\kappa \dot{M}}{4\pi v_\infty R} = 2.5 \frac{\kappa R_\odot}{\kappa_e R} \frac{\dot{M}_{-5}}{v_{1000}}. \quad (15.1)$$

The second, approximate equality here applies to the simple case of a steady, spherically symmetric wind with mass loss rate \dot{M} , and approximated for simplicity to flow at a constant speed v_∞ . The last equality uses the shorthand $\dot{M}_{-5} = \dot{M}/(10^{-5} M_\odot/\text{yr})$ and $v_{1000} = v_\infty/(1,000 \text{ km/s})$ to give numerical scalings in terms of the opacity for electron scattering, which for a fully ionized medium with standard hydrogen mass fraction, $X = 0.7$, has a CGS value $\kappa_e = 0.2(1+X) = 0.34 \text{ cm}^2/\text{g}$. For example, electron scattering in the solar wind has $\tau_* \approx 10^{-8}$, confirming it is very transparent. But the winds from Wolf-Rayet stars, with a billion times higher \dot{M} , can become optically thick, even to electron scattering.

For the strong, slow winds from cool giants, the fraction of free electrons becomes small, but the cool, dense conditions often allow molecules and even dust to form. Spherical dust of radius a , mass m_d , density ρ_d has a physical cross section $\sigma = 3m_d/4a\rho_d$; conversion of a mass fraction X_d of wind material into dust thus implies an overall opacity $\kappa_d = 3X_d/4a\rho_d$. For standard (solar) abundances, $X_d \approx 2 \times 10^{-3}$, and since $\rho_d \sim 1 \text{ g/cm}^3$ (most dust would almost float in water), it is seen that for dust grains with typical size $a \approx 0.1 \mu$, the corresponding opacity is of order $\kappa_d \approx 100 \text{ cm}^2/\text{g}$, several hundred times greater than for free-electron scattering.

This geometric cross section only applies to wavelengths much smaller than the dust size, $\lambda \ll a$; for $\lambda \geq a$, the associated dust opacity decreases as $\kappa_d(\lambda) \sim (\lambda/a)^{-\beta}$, where $\beta = 4$ for simple Rayleigh scattering from smooth spheres of fixed size a . In practice, the complex mixtures in sizes and shapes of dust typically lead to a smaller effective power index, $\beta \approx 1-2$. Still, the overall inverse dependence on wavelength means that winds that are optically thick to dust absorption and scattering can show a substantially reddened spectrum.

Moreover, the energy from dust-absorbed optical light is generally reemitted in the infrared (IR), at wavelengths set by the dust temperature through roughly the standard Wien's law for peak emission of a blackbody, $\lambda = 2.90 \mu\text{m}/(T/1,000 \text{ K})$. For typical dust temperatures of several hundreds to a thousand degrees, this gives a strong IR excess in emission peaking in the 3–10 μm range. Such IR excess signatures of wind dust are seen in very cool-giant stars, particularly the so-called Carbon stars, but also in the much hotter Carbon-type Wolf-Rayet stars, known as WC stars. A good overview of dust opacity and emission is given by Li (2005).

2.2.2 Doppler-Shifted Line Absorption

It is much more common for winds to become optically thick to *line* absorption or scattering that results from transitions between two bound levels of an atom (including ions), or molecule. Because this is a *resonant* process, the associated cross sections and opacities can be much larger than from free-electron scattering, enhanced by factor that depends on the “quality” of the resonance.¹ For atomic transitions, classical calculations (i.e., without quantum mechanics) show the resonance enhancement factor is given roughly by $q = A\lambda_o/r_e$, where A is the mass abundance fraction of the atom, λ_o is the photon wavelength for the line transition, and $r_e = e^2/m_e c^2 = 2.6 \times 10^{-13}$ cm is the classical radius for electron charge e and mass m_e (Gayley 1995). For ultraviolet line transitions with $\lambda_o \approx 250$ nm and from abundant ions with $A \approx 10^{-5}$, we find $q \approx 10^3$.

As measured in the *rest frame* of the ion, this line opacity is confined to a very narrow range around the resonant wavelength λ_o . But the Doppler shift from the ion’s random thermal motion gives lines a finite Doppler width $\Delta\lambda_D = \lambda_o v_{th}/c$, where for ions with atomic mass m_i and temperature T , the thermal speed $v_{th} = \sqrt{kT/m_i}$. For typical observed ions of carbon, nitrogen, and oxygen (CNO) in a hot-star wind with temperatures a few times 10^4 K, we find $v_{th} \approx 10$ km/s.

In a stellar wind with flow speed $v \approx 1,000$ km/s $\gg v_{th}$, the Doppler shift from the wind flow completely dominates this thermal broadening. As illustrated in [Fig. 15-3](#), a stellar photon of wavelength $\lambda < \lambda_o - \Delta\lambda_D$ emitted radially from the star thus propagates freely through the wind until reaching a location where the wind speed v has shifted the line into resonance with the

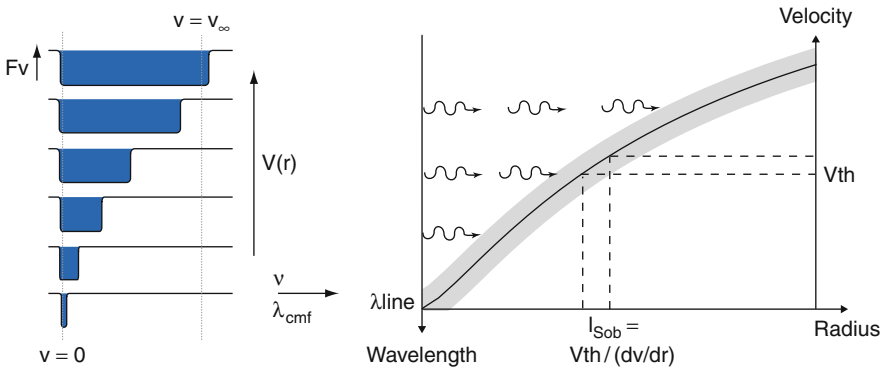


Fig. 15-3

Two perspectives for the Doppler-shifted line resonance in an accelerating flow. *Right:* Photons with a wavelength just shortward of a line propagate freely from the stellar surface up to a layer where the wind outflow Doppler shifts the line into a resonance over a narrow width (Represented here by the shading) equal to the Sobolev length, set by the ratio of thermal speed to velocity gradient, $l_{Sob} \equiv v_{th}/(dv/dr)$. *Left:* Seen from successively larger radii within the accelerating wind, the Doppler shift sweeps out an increasingly broadened line-absorption trough blueward of line center in the stellar spectrum

¹The effect is somewhat analogous to blowing into a whistle vs. just into open air. Like the sound of whistle, the response occurs at a well-tuned frequency, and has a greatly enhanced strength.

photon,

$$\lambda = \lambda'_o \equiv \lambda_o(1 - v/c). \quad (15.2)$$

The width of this resonance is given by $l_{Sob} = v_{th}/(dv/dr)$, known as the Sobolev length, after the Russian astrophysicist V. V. Sobolev, who first developed the theory for line radiation transport in such high-speed outflows (Sobolev 1957, 1960). For a wind of terminal speed v_∞ from a star of radius R , a characteristic velocity gradient is $dv/dr \approx v_\infty/R$, implying $l_{Sob}/R \approx v_{th}/v_\infty \approx 0.01 \ll 1$, and so showing this Sobolev line resonance is indeed quite sharp and narrow.

The *Sobolev approximation* assumes a narrow-line limit $v_{th} \rightarrow 0$ to derive localized, analytic solutions for the line transport, using the fact that the opacity then becomes nearly a δ -function about the local resonant wavelength, $\kappa(\lambda) = q\kappa_e\delta(\lambda/\lambda_o - 1 + v/c)$. For wavelengths from line center λ_o to a blue-edge $\lambda_\infty \equiv \lambda_o(1 - v_\infty/c)$, the associated wind optical depth then becomes

$$\tau(\lambda) = \int_R^\infty \kappa(\lambda)\rho dr = \left[\frac{q\kappa_e\rho c}{dv/dr} \right]_{res} \equiv \tau_{Sob}, \quad (15.3)$$

where in the second equality the wind quantities are to be evaluated at the relevant resonance radius where $v(r_{res}) \equiv c(1 - \lambda/\lambda_o)$.

As a simple explicit example, for a steady wind with a canonical wind velocity law $v(r) = v_\infty(1 - R/r)$, we find

$$\tau(\lambda) = \frac{\tau_o}{1 - R/r_{res}} = \frac{\tau_o v_\infty}{c(1 - \lambda/\lambda_o)}, \quad (15.4)$$

where

$$\tau_o \equiv \frac{q\kappa_e\dot{M}c}{4\pi Rv_\infty^2} = \frac{qc}{v_\infty}\tau_{*,e}. \quad (15.5)$$

The latter equality in (15.5) emphasizes that this *line* optical depth is a factor qc/v_∞ larger than the *continuum* optical depth for electron scattering, as given by (15.1). For strong lines ($q \approx 1,000$), and even for moderately fast winds with $v_\infty \approx 1,000$ km/s, this enhancement factor can be several *millions*. For winds with $v_\infty \approx 1,000$ km/s and $R \approx 10^{12}$ cm, such strong lines would be optically thick for mass loss rates as low as $\dot{M} \sim 10^{-10} M_\odot/\text{yr}$; for dense winds with $\dot{M} \sim 10^{-6} M_\odot/\text{yr}$, strong lines can be *very* optically thick, with $\tau_o \sim 10^4$!

Defining a wind-scaled wavelength displacement from line center, $x \equiv (c/v_\infty)(\lambda/\lambda_o - 1)$, (15.4) gives the very simple wavelength scaling, $\tau(x) = \tau_o/(-x)$. For a simple “point-source” model (which ignores the finite size of the star and so assumes that all radiation is radially streaming), this predicts the observed stellar flux spectrum should show a blueward line-absorption trough of the form,

$$F(x) = F_c e^{-\tau_o/|x|}; \quad -1 < x < 0, \quad (15.6)$$

where F_c is the stellar continuum flux far away from the line. (For the somewhat more general velocity law $v(r) = v_\infty(1 - R/r)^\beta$, the optical depth scaling becomes $\tau(x) = \tau_o/\beta|x|^{2-1/\beta}$.)

2.2.3 Asymmetric P-Cygni Profiles from Scattering Lines

Strong spectral lines often tend to *scatter* rather than fully absorb stellar radiation, and this leads to the emergent line profile developing a very distinctive form known as a “P-Cygni profile,”

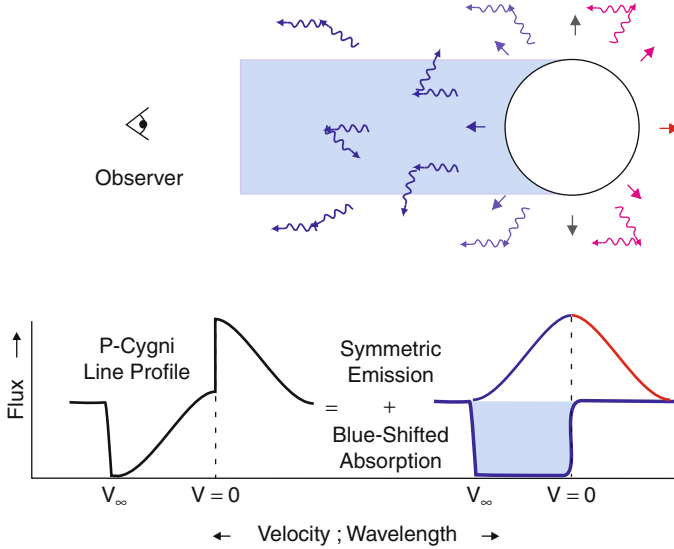


Fig. 15-4
Schematic illustration of the formation of a P-Cygni type line profile in an expanding wind outflow

after the star P Cygni for which its significance as a signature of mass outflow was first broadly recognized.

Figure 15-4 illustrates the basic principles for formation of such a P-Cygni line profile. Wind material approaching an observer within a column in front of the star has its line resonance blueshifted by the Doppler effect. Thus scattering of stellar radiation out of this direction causes an absorption trough on the blue side of the line profile, much as described in the simple, pure-absorption analysis given above. However, from the lobes on either side of this absorption column, wind material can also scatter radiation toward the observer. Since this can occur from either the approaching or receding hemisphere, this scattered radiation can be either blueshifted or redshifted. The associated extra flux seen by the observer thus occurs as a symmetric emission component on both sides of the line center. Combined with the reduced blue-side flux, the overall profile has a distinctly asymmetric form, with apparent net blueward absorption and redward emission.

Derivations of the full equations are given, e.g., in Mihalas (1978) and Lamers and Cassinelli (1999), but a brief outline of the quantitative derivation is as follows.

First, the above point-star computation of the absorption trough from stellar light scattered out of the line of sight to the observer must now be generalized to account for rays parallel to the radial ray to the observer, but offset by a distance p , with $0 \leq p \leq R$. Denoting z as the coordinate along such rays, with $z = 0$ at the midplane where the rays come closest the star's center, then the optical depth from the star (at $z_* = \sqrt{R^2 - p^2}$) to the observer (at $z \rightarrow +\infty$) is (cf. [15.3])

$$\tau(p, \lambda) = \int_{z_*}^{\infty} \kappa(\lambda) \rho dz = \left[\frac{q \kappa_e \rho c}{dv_z/dz} \right]_{res} . \tag{15.7}$$

The resonance condition is now $v_z(z_{res}) \equiv c(1 - \lambda/\lambda_0) = -v_\infty x$, with the ray projection of the radial wind speed given by $v_z = \mu v$, where $\mu = z/\sqrt{z^2 + p^2}$. Written in terms of the wind-scaled wavelength $x \equiv (c/v_\infty)(\lambda/\lambda_0 - 1)$, the observed *direct* intensity is thus attenuated from the stellar surface value,

$$I_{dir}(p, x) = I_c e^{-\tau(p, x)}, \quad (15.8)$$

which upon integration over the stellar core gives for the observed direct flux (cf. [► 15.6])

$$F_{dir}(x) = F_c \int_0^R e^{-\tau(p, x)} \frac{2p dp}{R^2}. \quad (15.9)$$

For the scattered, emission component, the formal solution of radiative transfer (Mihalas 1978) takes a purely local form within the Sobolev approximation,

$$I_{scat}(p, x) = S \left(1 - e^{-\tau(p, x)} \right), \quad (15.10)$$

where the source function S for pure-scattering is given by the wavelength- and angle-averaged mean intensity, customarily denoted \bar{J} . In static atmospheres, computing this source function requires a *global* solution of the line scattering, but in an expanding wind, methods developed by Sobolev (1960) allow it to be computed in terms of purely *local* “escape probabilities.” Overall, the radial scaling follows roughly the optically thin form for diluted core radiation $S_{thin} = WI_c$, where the dilution factor $W \equiv (1 - \mu_*)/2$, with $\mu_* \equiv \sqrt{1 - R^2/r^2}$. The observed scattered flux is then computed from integration over all suitable rays,

$$F_{scat}(x) = \frac{2\pi}{r^2} \int_{p_{min}}^\infty I_{scat}(p, x) p dp, \quad (15.11)$$

where $p_{min} = R$ for red-side wavelengths ($\lambda > \lambda_0$) that scatter from the back hemisphere that is occulted by the star, and $p_{min} = 0$ otherwise.

The total observed flux, $F(x) = F_{dir}(x) + F_{scat}(x)$, combines the blueshifted absorption of the direct component plus the symmetric emission of the scattered component, yielding then the net asymmetry of the P-Cygni profile shown in ► Fig. 15-4 and ► Fig. 15-5.

The quantitative fitting of observed line profiles often uses the so-called SEI (Sobolev with Exact Integration) method (Lamers et al. 1987; Groenewegen and Lamers 1989), in which the Sobolev approximation is only used for computation of the scattering source function, which as a wavelength- and angle-averaged quantity tends to cancel errors associated with the finite width of the line resonance. However, because *microturbulence* in a stellar wind can effectively broaden that resonance to many (factor ten or more) times the thermal value $v_{th} \approx 10$ km/s, an exact integration over depth is used for the formal solution of line transfer.

Measurements of the blue-edge of a strong absorption trough immediately gives the wind terminal speed. Moreover, if the line is detectable but not saturated (i.e., $0.1 < \tau_0 < 3$), then the observed depth of the trough can in principal be used to infer \dot{M} , assuming one knows the line opacity. In practice, uncertainties in the ionization fraction of prominent ions, which feed directly into the opacity strength factor q , often limit the utility of this method.

But recent *FUSE* observations of UV lines from P^{+4} (a k a PV) have proven particularly useful for inferring mass loss rates of O stars (Fullerton et al. 2006). Because PV is often nearly the dominant ionization stage, the ionization correction is less uncertain. Moreover, the low elemental abundance of phosphorus means that the lines, unlike those from more abundant elements, are not generally saturated. Finally, in contrast to density-squared diagnostics, line

scattering is a single-density process, and so is not affected by the degree of wind clumping. Indeed, mass loss rates inferred by this method tend to be substantially lower, by a factor of 10 or more, compared to those inferred from the density-squared diagnostics discussed in the next subsections (Fullerton et al. 2006). The resolution of this mass loss discrepancy is matter of much current research and discussion (see, e.g., Puls et al. 2006 and Hamann et al. 2008).

2.2.4 Wind-Emission Lines

In WR stars with very dense winds, the emergent spectrum is characterized by very broad (>1,000 km/s Doppler width) emission lines from various ionization stages of abundant elements like He, N, C, and O. The recombination of an electron and ion generally occurs through a downward cascade through the many bound levels of the ion, giving the bound-bound line emission. The involvement of an ion plus free electron means this is one of the processes that scale with the *square* of the gas density. In the narrow-line (Sobolev) approximation, the *line emissivity* (energy per unit time, volume, and solid angle) at wind-scaled wavelength x and from some wind radius with velocity $v(r)$ is proportional to

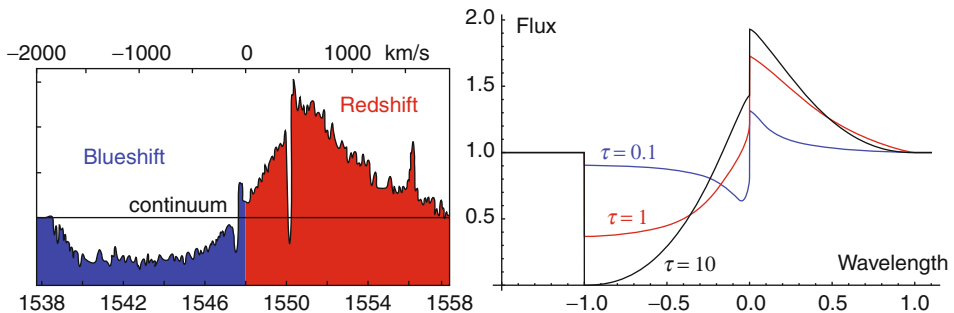
$$\eta(x, r, \mu) \propto \rho^2 \delta(x + \mu v(r)/v_\infty), \quad (15.12)$$

where μ is the direction cosine for the emitted radiation relative to the local radial direction. Integration over all directions μ then gives for the emission luminosity contribution from a narrow shell between r and $r + dr$,

$$\frac{dL(x)}{dr} \propto r^2 \rho^2 \int_{-1}^{+1} d\mu \delta(x + \mu v(r)/v_\infty) \quad (15.13)$$

$$\propto r^2 \rho^2 \frac{v_\infty}{v(r)} \quad \text{if } |x| \leq \frac{v(r)}{v_\infty} \quad (15.14)$$

$$= 0 \quad \text{otherwise.} \quad (15.15)$$



■ Fig. 15-5

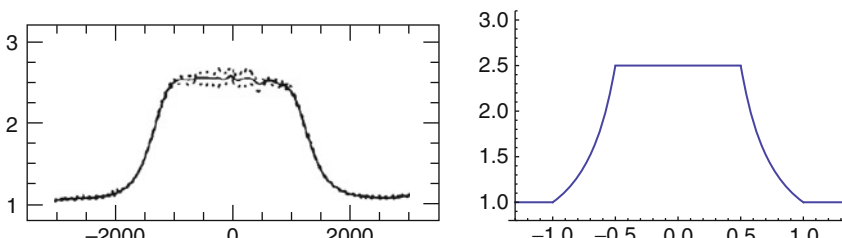
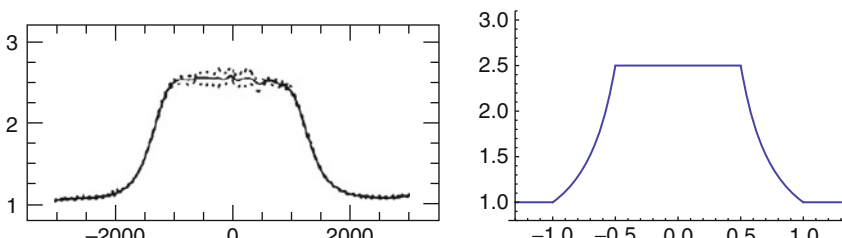
Left: Observed P-Cygni line profile for C^{+3} from NGC 6543, the central star in the “Cat’s Eye” nebula. **Right:** Theoretical P-Cygni profile for a wind with velocity law $v(r) = v_\infty (1 - R/r)$, plotted as flux vs. wind-scaled wavelength $x = (c/v_\infty)(\lambda/\lambda_o - 1)$; the three curves show results for a weak, moderate, and strong line, with characteristic line strengths (see (15.5)) $\tau_o = 0.1, 1, \text{ and } 10$

Thus each such shell produces a *flat-top* profile extending to $x = \pm v/v_\infty$ about line center. If the ionization stage to produce the emission does not form until near the wind terminal velocity, then the observed profile is indeed flat topped, with a half-width given by v_∞ .

But if the ion already forms at a lower radius with a velocity $v_{min} < v_\infty$, then the profile exhibits a flat-topped center for $|x| < v_{min}/v_\infty$, with tapered wings extending to $x = \pm 1$ (see, e.g., Dessart and Owocki 2003). For example, for the case of the standard velocity law $v(r) = v_\infty(1 - R/r)$, the emission at $|x| > v_{min}/v_\infty$ depends on the integral,

$$L(x) \propto \int \frac{\rho^2 r^2}{v} dr \propto \int \frac{dr}{v^3 r^2} \propto \int \frac{dx}{x^3} \propto \frac{1}{2x^2}, \quad (15.16)$$

where the second integrand follows from mass continuity, and the third uses the fact that $Rdr/r^2 = dv/v_\infty = -dx$. We thus obtain the simple analytic result that the line wing tapers off as $\log|x|$ from each side of the inner flat top over $|x| < v_{min}/v_\infty$.

Using this simple model, the right panel of  Fig. 15-6 plots a sample flat-top profile for $v_{min}/v_\infty = 0.5$. The left panel of  Fig. 15-6 (taken from Lepine and Moffat 1999) shows a corresponding observed profile, for the C III line from the star WR 134. The observed half-width of this emission line directly implies a wind speed of nearly 2,000 km/s for this star. Other WR stars show half-widths that imply wind speeds in the range 1,000–3,000 km/s.

Since the emission strength is proportional to $\rho^2 \sim \dot{M}^2$, careful modeling of the expanding wind and atmosphere can in principal enable one to use the observed strength of emission lines to also estimate the stellar mass loss rate. But such estimates depend on the wind velocity law, and, as noted above, on the degree of wind *clumping* (Hamann 1996; Hillier and Miller 1999; Hamann et al. 2003; Hillier 2003; Puls et al. 2006).

For O stars, a key mass loss rate diagnostic is the Balmer ($H\alpha$) line emission from the $n = 3$ to $n = 2$ transition of recombining Hydrogen (Puls et al. 1996). It tends to be dominated by emission very near the star, and so is not as sensitive to the wind terminal speed. As a ρ^2 diagnostic, it is also sensitive to wind clumping, but in this case, in the relatively low-speed flow near the stellar surface.

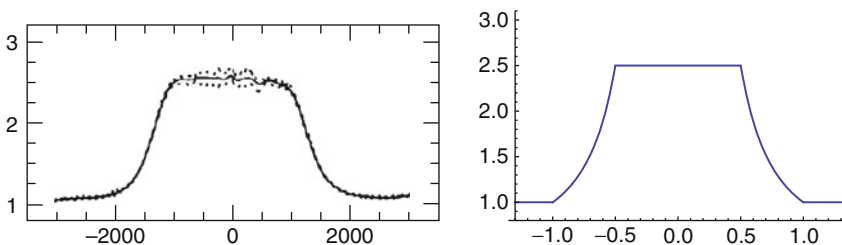


 Fig. 15-6

Left: Observed flat-top line profiles of twice ionized carbon C III ($\lambda 5,696 \text{ \AA}$) from the Wolf-Rayet star WR 137 (From Lepine and Moffat 1999), plotted vs. velocity-unit wavelength shift from line center. **Right:** Simple analytic flat-top emission line profile plotted vs. wind-scaled wavelength $x = (c/v_\infty)(\lambda/\lambda_o - 1)$; the model assumes a velocity law $v(r) = v_\infty(1 - R/r)$ with emission starting at a minimum speed $v_{min} = v_\infty/2$

2.2.5 Continuum Emission in Radio and Infrared

The dense, warm stellar winds from hot supergiants can also produce substantial continuum emission at radio and infrared (IR) wavelengths. Those with spectra showing a flux that increases with frequency are identified as “non-thermal,” and are now associated with binary systems wherein electrons accelerated in the shock collision between the two winds emit radio waves through gyration about the local magnetic field (van Loo et al. 2005).

More useful as a wind diagnostic are the *thermal* emitters, wherein the radio/IR arises from free-free emission by electrons with thermal energies characteristic of the wind temperature. A landmark analysis by Wright and Barlow (1975) showed how the observed flux of thermal radio/IR emission could be used as a quite direct diagnostic of the wind mass loss rate.

Both free-free emission and absorption are density-squared processes. For absorption in a wind moving at constant speed v_∞ , the radial optical depth from a radius r to the observer is thus given by

$$\tau_\nu(r) = K(\nu, T) \int_r^\infty \rho^2(r') dr' = K(\nu, T) \frac{\dot{M}^2}{48\pi^2 v_\infty^2 r^3}, \quad (15.17)$$

where the dependence on frequency ν and temperature T is set by $K(\nu, T) \sim \nu^{-2} T^{-3/2}$ (Allen 1973; Wright and Barlow 1975). Solving $\tau_\nu(R_\nu) = 1$ allows us to define a characteristic radius for the “radio/IR photosphere” at frequency ν ,

$$R_\nu = \left[K(\nu, T) \frac{\dot{M}^2}{48\pi^2 v_\infty^2} \right]^{1/3}. \quad (15.18)$$

For hot supergiants, the wind density is so high that this radio/IR photosphere can be at *hundreds* of stellar radii, $R_\nu > 100 R$.

The radio/IR luminosity can then be estimated by a simple model that accumulates the total outward emission from a sphere with this photospheric radius; since free-free emission is a thermal process, the surface brightness of this photosphere is set by the Planck function $B_\nu(T)$, giving

$$L_\nu = 2\pi B_\nu 4\pi R_\nu^2 = 8\pi^2 B_\nu \left[K(\nu, T) \frac{\dot{M}^2}{48\pi^2 v_\infty^2} \right]^{2/3} \quad (15.19)$$

For radio/IR frequencies and typical stellar wind temperatures, the Planck function is well approximated by its Rayleigh–Jeans form, $B_\nu \approx 2\nu^2 kT/c^2$. Using the above scaling for $K(\nu, T) \sim \nu^{-2} T^{-3/2}$, it is then seen that the radio/IR luminosity scales with frequency as $L_\nu \sim \nu^{2/3}$, but becomes *independent* of temperature.

The luminosity scales with wind parameters as $L_\nu \sim (\dot{M}/v_\infty)^{4/3}$, but otherwise depends just on known atomic constants. As such, if the wind terminal speed is known from other diagnostics, such as P-Cygni line profiles, measurements of the radio/IR flux can provide (for known stellar distance) a relatively robust diagnostic of the wind mass loss rate \dot{M} . But again, because of the scaling with density squared, in a clumped wind such radio/IR inferred mass loss rates are overestimated by a factor $C_f = 1/\sqrt{f_v}$, where now f_v is the clump volume filling factor in the distant, *outer* wind. Comparison with mass loss rates derived from $H\alpha$, which also scales with density squared but is formed near the star, can thus give a clue to the radial evolution of wind clumping (Puls et al. 2006).

3 General Equations and Formalism for Stellar Wind Mass Loss

With this background on wind diagnostics, let us now turn to theoretical modeling of stellar winds. This section lays the groundwork by defining the basic dynamical equations for conservation of mass, momentum, and energy. The following sections review the mechanisms for wind driving for the different types of stellar winds.

3.1 Hydrostatic Equilibrium in the Atmospheric Base of Any Wind

A stellar wind outflow draws mass from the large reservoir of the star at its base. In the star's atmosphere, the mass density ρ becomes so high that the net mass flux density ρv for the overlying steady wind requires only a very slow net drift speed v , much below the local sound speed. In this nearly static region, the gravitational acceleration \mathbf{g}_{grav} acting on the mass density ρ is closely balanced by a pressure gradient ∇P ,

$$\nabla P = \rho \mathbf{g}_{grav}, \quad (15.20)$$

a condition known as *hydrostatic equilibrium*. In luminous stars, this pressure can include significant contributions from the stellar radiation, but for now let us assume (as is applicable for the sun and other cool stars) it is set by the ideal gas law

$$P = \rho k T / \mu = \rho a^2. \quad (15.21)$$

The latter equality introduces the isothermal sound speed, defined by $a \equiv \sqrt{kT/\mu}$, with T the temperature, μ the mean atomic weight, and k Boltzmann's constant. The ratio of (15.21) to (15.20) defines a characteristic pressure scale height,

$$H \equiv \frac{P}{|\nabla P|} = \frac{a^2}{|g_{grav}|}. \quad (15.22)$$

In the simple ideal case of an isothermal atmosphere with constant sound speed a , this represents the scale for exponential stratification of density and pressure with height z

$$\frac{P(z)}{P_*} = \frac{\rho(z)}{\rho_*} = e^{-z/H}, \quad (15.23)$$

where the asterisk subscripts denote values at some surface layer where $z \equiv 0$. In practice, the temperature variations in an atmosphere are gradual enough that quite generally both pressure and density very nearly follow such an exponential stratification.

As a typical example, in the solar photosphere $T \approx 6,000$ K and $\mu \approx 10^{-24}$ g, yielding a sound speed $a \approx 9$ km/s. For the solar surface gravity $g_{grav} = GM_{\odot}/R_{\odot}^2 \approx 2.7 \times 10^4$ cm/s², this gives a pressure scale height of $H \approx 300$ km, which is very much less than the solar radius $R_{\odot} \approx 700,000$ km. This implies a sharp edge to the visible solar photosphere, with the emergent spectrum well described by a planar atmospheric model fixed by just two parameters – typically effective temperature and gravity – and not dependent on the actual solar radius.

This relative smallness of the atmospheric scale height is a key general characteristic of static stellar atmospheres, common to all but the most extremely extended giant stars. In general, for stars with mass M , radius R , and surface temperature T , the ratio of scale height to radius

can be written in terms of the ratio of the associated sound speed a_* to surface escape speed $v_e \equiv \sqrt{2GM/R}$,

$$\frac{H_*}{R} = \frac{2a_*^2}{v_e^2} \equiv 2s. \quad (15.24)$$

One recurring theme of this chapter is that the value of this ratio is also of direct relevance to stellar winds. The parameter $s \equiv (a_*/v_e)^2$ characterizes roughly the ratio between the gas internal energy and the gravitational escape energy. For the solar photosphere, $s \approx 2.2 \times 10^{-4}$, and even for very hot stars with an order of magnitude higher photospheric temperature, this parameter is still quite small, $s \sim 10^{-3}$. However, as discussed further in the next section, for the multimillion-degree temperature of the solar corona, this parameter is much closer to unity, and that is a key factor in the capacity for the thermal gas pressure to drive the outward coronal expansion that is the solar wind.

3.2 General Flow Conservation Equations

Let us now consider a case wherein a nonzero net force leads to a net acceleration,

$$\frac{d\mathbf{v}}{dt} = \frac{\partial \mathbf{v}}{\partial t} + \mathbf{v} \cdot \nabla \mathbf{v} = -\frac{\nabla P}{\rho} - \frac{GM}{r^2} \hat{\mathbf{r}} + \mathbf{g}_x. \quad (15.25)$$

Here \mathbf{v} is the flow velocity, \mathbf{g}_x is some yet-unspecified force-per-unit-mass, and the gravity is now cast in terms of its standard dependence on gravitation constant G , stellar mass M , and local radius r , with $\hat{\mathbf{r}}$ a unit radial vector.

Conservation of mass requires that any temporal change in the local density ρ must arise from a net divergence of the mass flux density $\rho \mathbf{v}$,

$$\frac{\partial \rho}{\partial t} + \nabla \cdot \rho \mathbf{v} = 0. \quad (15.26)$$

Conservation of internal energy takes a similar form, but now accounting also for any local sources or sinks of energy,

$$\frac{\partial e}{\partial t} + \nabla \cdot e \mathbf{v} = -P \nabla \cdot \mathbf{v} - \nabla \cdot \mathbf{F}_c + Q_x. \quad (15.27)$$

For an ideal gas with ratio of specific heats γ , the internal energy density e is related to the pressure through

$$P = \rho a^2 = (\gamma - 1)e. \quad (15.28)$$

On the right-hand-side of (15.27), Q_x represents some still unspecified, net volumetric heating or cooling, while \mathbf{F}_c is the conductive heat flux density, taken classically to depend on the temperature as

$$\mathbf{F}_c = -K_o T^{5/2} \nabla T, \quad (15.29)$$

where for electron conduction the coefficient $K_o = 5.6 \times 10^{-7}$ erg/s/cm/K^{7/2} (Spitzer 1962).

Collectively, (15.25)–(15.28) represent the general equations for a potentially time-dependent, multidimensional flow.

3.3 Steady, Spherically Symmetric Wind Expansion

In application to stellar winds, first-order models are commonly based on the simplifying approximations of steady-state ($\partial/\partial t = 0$), spherically symmetric, radial outflow ($\mathbf{v} = v\hat{r}$). The mass conservation requirement (● 15.26) can then be used to define a constant overall mass loss rate,

$$\dot{M} \equiv 4\pi\rho v r^2. \quad (15.30)$$

Using this and the ideal gas law to eliminate the density in the pressure gradient term then gives for the radial equation of motion

$$\left(1 - \frac{a^2}{v^2}\right) v \frac{dv}{dr} = -\frac{GM}{r^2} + \frac{2a^2}{r} - \frac{da^2}{dr} + g_x. \quad (15.31)$$

In general, evaluation of the sound-speed terms requires simultaneous solution of the corresponding, steady-state form for the flow energy, (● 15.27), using also the ideal gas law (● 15.28). But in practice, this is only of central importance for proper modeling of the pressure-driven expansion of a high-temperature (million-degree) corona, as discussed in the next section for the solar wind.

For stars without such a corona, any wind typically remains near or below the stellar photospheric temperature T , which as noted above implies a sound speed a_* that is much less than the surface escape speed v_e . This in turn implies that the sound-speed terms on the right-hand side of (● 15.31) are quite negligible, of order $s \equiv a_*^2/v_e^2 \sim 10^{-3}$ smaller than the gravity near the stellar surface. These terms are thus of little dynamical importance in determining the overall wind properties, like the mass loss rate or velocity law (see ● Sect. 4). However, it is still often convenient to retain the sound-speed term on the left-hand side, since this allows for a smooth mapping of the wind model onto a hydrostatic atmosphere through a subsonic wind base.

In general, to achieve a supersonic flow with a net outward acceleration, (● 15.31) shows that the net forces on the right-hand side must be positive. For coronal winds, this occurs by the sound-speed terms becoming bigger than gravity. For other stellar winds, overcoming gravity requires the additional body force represented by g_x , for example from radiation (● Sect. 5).

3.4 Energy Requirements of a Spherical Wind Outflow

In addition to these force or momentum conditions for a wind outflow, it is instructive to identify explicitly the general energy requirements. Combining the momentum and internal energy equations for steady, spherical expansion, we can integrate to obtain the *total energy* change from the base stellar radius R to some given radius r

$$\dot{M} \left[\frac{v^2}{2} - \frac{GM}{r} + \frac{\gamma}{\gamma-1} \frac{P}{\rho} \right]_R^r = \int_R^r (\dot{M}g_x + 4\pi r'^2 Q_x) dr' - 4\pi [r'^2 F_c]_R^r. \quad (15.32)$$

On the left-hand side, the terms represent the kinetic energy, gravitational potential energy, and internal enthalpy. To balance this, on the right-hand side are the work from the force g_x , the net volumetric heating Q_x , and the change in the conductive flux F_c . Even for the solar wind, the enthalpy term is generally much smaller than the larger of the kinetic or potential energy. Neglecting this term, evaluation at arbitrarily large radius $r \rightarrow \infty$ thus yields the approximate

requirement for the total energy per unit mass,

$$\frac{v_\infty^2}{2} + \frac{v_e^2}{2} \approx \int_R^\infty (g_x + 4\pi r'^2 Q_x / \dot{M}) dr' + \frac{4\pi R^2 F_{c*}}{\dot{M}}, \quad (15.33)$$

where F_{c*} is the conductive heat flux density at the coronal base, and it is assumed the outer heat flux vanishes far from the star. This equation emphasizes that a key general requirement for a wind is to supply the combined kinetic plus potential energy. For stellar winds, this typically occurs through the direct work from the force g_x . For the solar wind, it occurs through a combination of the volume heating and thermal conduction, as discussed next.

4 Coronal Expansion and Solar Wind

4.1 Reasons for Hot, Extended Corona

4.1.1 Thermal Runaway from Density and Temperature Decline of Line-Cooling

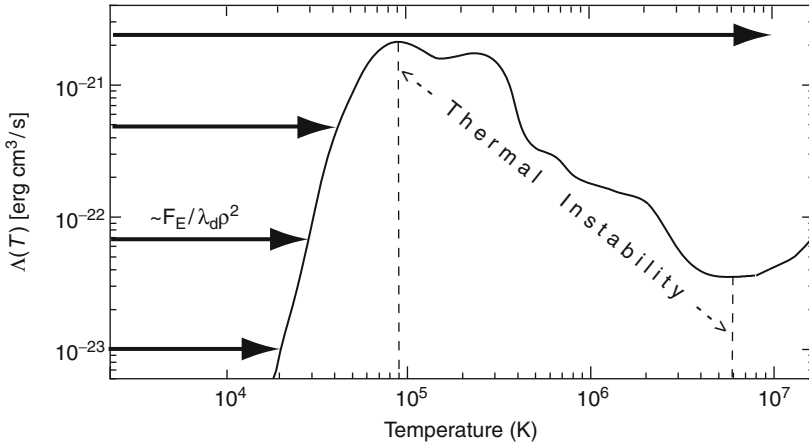
In the sun and other relatively cool stars, the existence of a strong near-surface convection zone provides a source of mechanical energy to heat the upper atmosphere and thereby *reverse* the vertical decrease of temperature of the photosphere. From photospheric values characterized by the effective temperature $T_{\text{eff}} \approx 6,000$ K, the temperature declines to a minimum $T_{\text{min}} \approx 4,000$ K, but then rises through a layer (the chromosphere) extending over many scale heights to about 10,000 K. Above this, it then jumps sharply across a narrow *transition region* of less than scale height, to values in the *corona* of order a *million* degrees! The high pressure associated with this high temperature eventually leads to the outward coronal expansion that is the solar wind.

This sharp jump in temperature is a direct result of the inability of the increasingly rarefied material in the upper atmosphere to radiate away any mechanical heating, for example associated with dissipation of some generic wave energy flux F_E over some damping length λ_d . To maintain a steady state with no net heating, this energy deposition must be balanced by radiative cooling, which can be taken to follow the scaling (e.g., Cox and Tucker 1969; Raymond et al. 1976),

$$\frac{F_E}{\lambda_d} = n_H n_e \Lambda(T). \quad (15.34)$$

Here $\Lambda(T)$ is known as the optically thin cooling function, which can be readily tabulated from a general atomic physics calculation for any assumed abundance of elements, with the standard result for solar (or “cosmic”) abundances plotted schematically in [Fig. 15-7](#). The overall scaling with the product of the hydrogen and electron number densities, n_H and n_e , reflects the fact that the radiative cooling arises from collisional excitation of ions by electrons, for the assumed abundance of ion species per hydrogen atom.

Consider then the nature of this energy balance within a hydrostatically stratified atmosphere, for which all the densities are declining *exponentially* in height z , with a scale height $H \ll R$. If the damping is linked to material absorption, it might scale inversely with density, but even so cooling would still scale with one higher power of density. Using [\(15.34\)](#), one



■ Fig. 15-7

Radiative cooling function $\Lambda(T)$ plotted vs. temperature T on a log–log scale. The arrows from the left represent the density-scaled rate of energy deposition, which increases with the exponential decrease in density with height. At the point where this scaled heating exceeds the maximum of the cooling function, the radiative equilibrium temperature jumps to a much higher value, in excess of 10^7 K

thus finds the radiative cooling function needs to increase exponentially with height

$$\Lambda[T(z)] \sim \frac{F_E}{\lambda_d \rho^2} \sim F_E e^{+z/H}. \quad (15.35)$$

As illustrated in **Fig. 15-7**, for any finite wave flux this required increase should lead to a steadily higher temperature until, upon reaching the local maximum of the cooling function at a temperature of ca. 10^5 K, a radiative balance can no longer be maintained without a drastic jump to very much higher temperature, above 10^7 K.

This *thermal instability* is the direct consequence of the decline in cooling efficiency above 10^5 K, which itself is an intrinsic property of radiative cooling, resulting from the progressive ionization of those ion stages that have the bound electrons needed for line emission. The characteristic number density at which runaway occurs can be estimated as

$$n_{run} \approx \sqrt{\frac{F_E}{\lambda_d \Lambda_{max}}} \approx 3.8 \times 10^7 \text{ cm}^{-3} \sqrt{\frac{F_5 R_\odot}{\lambda_h}} \quad (15.36)$$

where $\Lambda_{max} \approx 10^{-21} \text{ erg cm}^3/\text{s}$ is the maximum of the cooling function (see **Fig. 15-7**). The latter equality evaluates the scaling in terms of typical solar values for damping length $\lambda_d \approx R_\odot$ and wave energy flux density $F_5 = F_E/10^5 \text{ erg/cm}^2/\text{s}$. This is roughly comparable to the inferred densities at the base of the solar corona, that is, just above the top of the transition region from the chromosphere.

4.1.2 Coronal Heating with a Conductive Thermostat

In practice, the outcome of this temperature runaway of radiative cooling tends to be tempered by conduction of heat back into the cooler, denser atmosphere. Instead of the tens of million degrees needed for purely radiative restabilization, the resulting characteristic coronal temperature is “only” a few million degrees. To see this temperature scaling, consider a simple model in which the upward energy flux F_E through a base radius R is now balanced at each coronal radius r purely by downward conduction,

$$4\pi r^2 F_E = 4\pi r^2 K_o T^{5/2} \frac{dT}{dr}. \quad (15.37)$$

Integration between the base radius R and an assumed energy deposition radius R_d yields a characteristic peak coronal temperature

$$T \approx \left[\frac{7}{2} \frac{F_E}{K_o} \frac{R_d - R}{R_d/R} \right]^{2/7} \approx 2 \times 10^6 K F_5^{2/7}, \quad (15.38)$$

where the latter scaling applies for a solar coronal case with $R = R_\odot$ and $R_d = 2R_\odot$. This is in good general agreement with observational diagnostics of coronal electron temperature, which typically give values near 2 MK.

Actually, observations (Cranmer et al. 1999; Kohl et al. 1999) of the “coronal hole” regions thought to be the source of high-speed solar wind suggest that the temperature of *protons* can be significantly higher, about 4–5 MK. Coronal holes are very low density regions wherein the collisional energy coupling between electrons and protons can be insufficient to maintain a common temperature. For complete decoupling, an analogous conductive model would then require that energy added to the proton component must be balanced by its *own* thermal conduction. But because of the higher mass and thus lower thermal speed, proton conductivity is reduced by the root of the electron/proton mass ratio, $\sqrt{m_e/m_p} \approx 43$, relative to the standard electron value used above. Application of this reduced proton conductivity in (15.38) thus yields a proton temperature scaling

$$T_p \approx 5.8 \times 10^6 K F_5^{2/7}, \quad (15.39)$$

where now $F_5 = F_{Ep}/10^5 \text{ erg/cm}^2/\text{s}$, with F_{Ep} the base energy flux associated with proton heating. (15.39) matches better with the higher inferred proton temperature in coronal holes, but more realistically, modeling the proton energy balance in such regions must also account for the energy losses associated with coronal expansion into the solar wind (see Sect. 3.3).

4.1.3 Incompatibility of Hot Extended Hydrostatic Corona with ISM Pressure

Since the thermal conductivity increases with temperature as $T^{5/2}$, the high characteristic coronal temperature also implies a strong *outward* conduction flux F_c . For a conduction-dominated energy balance, this conductive heat flux has almost zero divergence,

$$\nabla \cdot \mathbf{F}_c = \frac{1}{r^2} \frac{d(r^2 K_o T^{5/2} (dT/dr))}{dr} \approx 0. \quad (15.40)$$

Upon double integration, this gives a temperature that declines only slowly outward from its coronal maximum, that is, as $T \sim r^{-2/7}$. The overall point thus is that, once a coronal base

is heated to a very high temperature, thermal conduction should tend to extend that high temperature outward to quite large radii (Chapman 1961).

This radially extended high temperature of a corona has important implications for the dynamical viability of maintaining a hydrostatic stratification. First, for such a high temperature, (☛ 15.24) shows that the ratio of scale height to radius is no longer very small. For example, for the typical solar coronal temperature of 2 MK, the scale height is about 15% of the solar radius. In considering a possible hydrostatic stratification for the solar corona, it is thus now important to take explicit account of the radial decline in gravity,

$$\frac{d \ln P}{dr} = -\frac{GM}{a^2 r^2}. \quad (15.41)$$

Motivated by the conduction-dominated temperature scaling $T \sim r^{-2/7}$, let us consider a slightly more general model for which the temperature has a power-law radial decline, $T/T = a^2/a_*^2 = (r/R)^{-q}$. Integration of (☛ 15.41) then yields

$$\frac{P(r)}{P_*} = \exp\left(\frac{R}{H_*(1-q)} \left[\left(\frac{R}{r}\right)^{1-q} - 1\right]\right), \quad (15.42)$$

where $H_* \equiv a_*^2 R^2 / GM$. A key difference from the exponential stratification of a nearly planar photosphere (cf. [☛ 15.23]) is that the pressure now approaches a *finite* value at large radii $r \rightarrow \infty$,

$$\frac{P_\infty}{P_*} = e^{-R/H_*(1-q)} = e^{-14/T_6(1-q)}, \quad (15.43)$$

where the latter equality applies for solar parameters, with T_6 the coronal base temperature in units of 10^6 K. This gives $\log(P_*/P_\infty) \approx 6/T_6(1-q)$.

To place this in context, note that a combination of observational diagnostics give $\log(P_{TR}/P_{ISM}) \approx 12$ for the ratio between the pressure in the transition region base of the solar corona and that in the interstellar medium. This implies that a hydrostatic corona could only be contained by the interstellar medium if $(1-q)T_6 < 0.5$. Specifically, for the conduction-dominated temperature index $q = 2/7$, this requires $T_6 < 0.7$. Since this is well below the observational range $T_6 \approx 1.5\text{--}3$, the implication is that a conduction-dominated corona cannot remain hydrostatic, but must undergo a continuous expansion, known of course as the solar wind.

But it is important to emphasize here that this classical and commonly cited argument for the “inevitability” of the solar coronal expansion depends crucially on *extending* a high temperature at the coronal base far outward. For example, a base temperature in the observed range $T_6 = 1.5\text{--}3$ would still allow a hydrostatic match to the interstellar medium pressure if the temperature were to decline with just a somewhat bigger power index $q = 2/3 - 5/6$.

4.2 Isothermal Solar Wind Model

These problems with maintaining a hydrostatic corona motivate consideration of dynamical wind solutions (Parker 1963). A particularly simple example is that of an *isothermal*, steady-state, spherical wind, for which the equation of motion [from (☛ 15.31), without external driving ($g_x = 0$) or sound-speed gradient ($da^2/dr = 0$)] becomes

$$\left(1 - \frac{a^2}{v^2}\right) v \frac{dv}{dr} = \frac{2a^2}{r} - \frac{GM}{r^2}, \quad (15.44)$$

Recall that this uses the ideal gas law for the pressure $P = \rho a^2$, and eliminates the density through the steady-state mass continuity; it thus leaves *unspecified* the constant overall mass loss rate $\dot{M} \equiv 4\pi\rho v r^2$.

The right-hand side of (15.44) has a zero at the critical radius

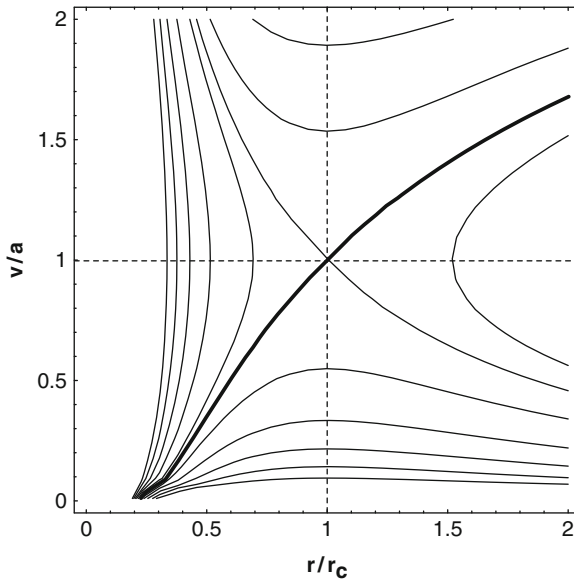
$$r_c = \frac{GM}{2a^2}. \quad (15.45)$$

At this radius, the left-hand side must likewise vanish, either through a zero velocity gradient $dv/dr = 0$, or through a sonic flow speed $v = a$. Direct integration of (15.44) yields the general solution

$$F(r, v) \equiv \frac{v^2}{a^2} - \ln \frac{v^2}{a^2} - 4 \ln \frac{r}{r_c} - \frac{4r_c}{r} = C, \quad (15.46)$$

where C is an integration constant. Using a simple contour plot of $F(r, v)$ in the velocity-radius plane, Fig. 15-8 illustrates the full “solution topology” for an isothermal wind. Note for $C = -3$, two contours cross at the critical radius ($r = r_c$) with a sonic flow speed ($v = a$). The positive slope of these represents the standard solar wind solution, which is the only one that takes a subsonic flow near the surface into a supersonic flow at large radii.

Of the other initially subsonic solutions, those lying above the critical solution fold back and terminate with an infinite slope below the critical radius. Those lying below remain subsonic everywhere, peaking at the critical radius, but then declining to arbitrarily slow, very subsonic



■ Fig. 15-8

Solution topology for an isothermal coronal wind, plotted via contours of the integral solution (15.46) with various integration constants C , as a function of the ratio of flow speed to sound speed v/a , and the radius over critical radius r/r_c . The heavy curve drawn for the contour with $C = -3$ represents the transonic solar wind solution

speeds at large radii. Because such subsonic “breeze” solutions follow a nearly *hydrostatic* stratification (Chamberlain 1961), they again have a large, finite asymptotic pressure that does not match the required interstellar boundary condition.

In contrast, for the solar wind solution the supersonic asymptotic speed means that, for any finite mass flux, the density, and thus the pressure, asymptotically approaches zero. To match a small, but finite interstellar medium pressure, the wind can undergo a shock jump transition onto one of the declining subsonic solutions lying above the decelerating critical solution.

Note that, since the density has scaled out of the controlling equation of motion (15.44), the wind mass loss rate $\dot{M} \equiv 4\pi\rho v r^2$ does not appear in this isothermal wind solution. An implicit assumption hidden in such an isothermal analysis is that, no matter how large the mass loss rate, there is some source of heating that counters the tendency for the wind to cool with expansion. As discussed below, determining the overall mass loss rate requires a model that specifies the location and overall level of this heating.

4.2.1 Temperature Sensitivity of Mass Loss Rate

This isothermal wind solution does nonetheless have some important implications for the *relative* scaling of the wind mass loss rate. To see this, note again that within the *subsonic* base region, the inertial term on the left side of (15.44) is relatively small, implying the subsonic stratification is nearly hydrostatic. Thus, neglecting the inertial term v^2/a^2 in the isothermal solution (15.46) for the critical wind case $C = -3$, one can solve approximately for the *surface* flow speed

$$v_* \equiv v(R) \approx a \left(\frac{r_c}{R} \right)^2 e^{3/2 - 2r_c/R}. \quad (15.47)$$

Here “surface” should really be interpreted to mean at the base the hot corona, that is, just above the chromosphere–corona transition region.

In the case of the sun, observations of transition region emission lines provide a quite tight empirical constraint on the gas *pressure* P_* at this near-surface coronal base of the wind (Withbroe 1988). Using this and the ideal gas law to fix the associated base density $\rho_* = P_*/a^2$, one finds that (15.47) implies a mass loss scaling

$$\dot{M} \equiv 4\pi\rho_* v_* R^2 \approx 56 \frac{P_*}{a} r_c^2 e^{-2r_c/R} \propto \frac{P_*}{T_6^{5/2}} e^{-14/T_6}. \quad (15.48)$$

With $T_6 \equiv T/10^6$ K, the last proportionality applies for the solar case, and is intended to emphasize the steep, exponential dependence on the inverse temperature. For example, assuming a fixed pressure, just doubling the coronal temperature from one to two million degrees implies nearly a factor 200 increase in the mass loss rate!

Even more impressively, decreasing from such a 1 MK coronal temperature to the *photospheric* temperature $T \approx 6,000$ K would decrease the mass loss rate by more than a *thousand orders of magnitude!* This reiterates quite strongly that thermally driven mass loss is completely untenable at photospheric temperatures.

The underlying reason for this temperature sensitivity stems from the exponential stratification of the subsonic coronal density between the base radius R and the sonic/critical radius r_c . From (15.24) and (15.45) it is clear that this critical radius is closely related to the ratio of

the base scale height to stellar radius

$$\frac{r_c}{R} = \frac{R}{2H} = \frac{v_e^2}{4a^2}, \quad (15.49)$$

where the latter equality also recalls the link with the ratio of sound speed to surface escape speed. Application in (● 15.48) shows that the argument of the exponential factor simply represents the number of base scale heights within a critical radius.

As noted in ● Sect. 2.1, in situ measurements by interplanetary spacecraft show that the solar wind mass flux is actually quite constant, varying only by about a factor of 2 or so. In conjunction with the predicted scalings like (● 15.48), and the assumption of fixed based pressure derived from observed transition region emission, this relatively constant mass flux has been viewed as requiring a sensitive *fine-tuning* of the coronal temperature (e.g., Leer and Holzer 1979; Withbroe 1989).

4.2.2 The Solar Wind as a Thermostat for Coronal Heating

But a more appropriate perspective is to view this temperature-sensitive mass loss as providing an effective way to *regulate* the temperature resulting from coronal heating. This can be seen by considering explicitly the energy requirements for a thermally driven coronal wind. From (● 15.32) (with $g_x = 0$), the total energy change from a base radius R to a given radius r is

$$\dot{M} \left[\frac{v^2}{2} - \frac{v_e^2 R}{2r} + \frac{\gamma a^2}{\gamma - 1} \right]_R^r = 4\pi \int_R^r r'^2 Q_x dr' + 4\pi [R^2 F_{c*} - r^2 F_c]. \quad (15.50)$$

The expression here of the gravitational and internal enthalpy in terms of the associated escape and sound speed v_e and a allows convenient comparison of the relative magnitudes of these with the kinetic energy term, $v^2/2$. Even at typical coronal temperature of 2 MK, the enthalpy term is only about a third of the gravitational escape energy from the solar surface, implying that the initially slow, subsonic flow at the wind base has negative total energy set by gravity. Far from the star, this gravitational term vanishes, and the kinetic energy associated with the supersonic solar wind dominates. Since enthalpy is thus not important in either limit, let us for convenience ignore its relatively minor role in the global wind energy balance, giving then

$$E_w \equiv \dot{M} \left(\frac{v_\infty^2}{2} + \frac{v_e^2}{2} \right) \approx 4\pi \int_R^\infty r'^2 Q_x dr' + 4\pi R^2 (F_{c*}). \quad (15.51)$$

Here the outer heat flux is assumed to vanish asymptotically far from the star, while $F_{c*} < 0$ is the (inward) conductive heat flux density at the coronal base. ● Equation 15.51 shows then that the total energy of the solar wind is just given by the total, volume-integrated heating of the solar corona and wind, minus the lost energy by conduction back into the solar atmosphere. The analysis in ● Sect. 4.1.3 discussed how the heating of a strictly static corona can be balanced by the inward conductive flux back into the sun. But (● 15.51) now shows that an outflowing corona allows a net difference in heating minus conduction to be carried outward by the solar wind.

In this sense, the problem of “fine-tuning” the coronal temperature to give the observed, relatively steady mass flux is resolved by a simple change of perspective, recognizing instead that for a given level of coronal heating, the strongly temperature-sensitive mass and energy loss of the solar wind provides a very effective “thermostat” for the coronal temperature.

4.3 Driving High-Speed Streams

More quantitative analyses solve for the wind mass loss rate and velocity law in terms of some model for both the level and spatial distribution of energy addition into the corona and solar wind. The specific physical mechanisms for the heating are still a matter of investigation, but one quite crucial question regards the relative fraction of the total base energy flux deposited in the subsonic vs. supersonic portion of the wind. Models with an explicit energy balance generally confirm a close link between mass loss rate and energy addition to the subsonic base of coronal wind expansion. By contrast, in the supersonic region this mass flux is essentially fixed, and so any added energy there tends instead to increase the energy per mass, as reflected in asymptotic flow speed v_∞ (Leer et al. 1982).

A important early class of solar wind models assumed some localized deposition of energy very near the coronal base, with conduction then spreading that energy both downward into the underlying atmosphere and upward into the extended corona. As noted, the former can play a role in regulating the coronal base temperature, while the latter can play a role in maintaining the high coronal temperature needed for wind expansion. Overall, such conduction models of solar wind energy transport were quite successful in reproducing interplanetary measurements of the speed and mass flux of the “quiet,” low-speed ($v_\infty \approx 350\text{--}400$ km/s) solar wind.

However, such models generally fail to explain the high-speed ($v_\infty \approx 700$ km/s) wind streams that are inferred to emanate from solar “corona holes.” Such coronal holes are regions where the solar magnetic field has an open configuration that, in contrast to the closed, nearly static coronal “loops,” allows outward, radial expansion of the coronal gas. To explain the high-speed streams, it seems that some substantial fraction of the mechanical energy propagating upward through coronal holes must not be dissipated as heat near the coronal base, but instead must reach upward into the supersonic wind, where it provides either a direct acceleration (e.g., via a wave pressure that gives a net outward g_x) or heating ($Q_x > 0$) that powers extended gas-pressure acceleration to high speed.

Observations of such coronal hole regions from the SOHO satellite (Cranmer et al. 1999; Kohl et al. 1999) show temperatures of $T_p \approx 4\text{--}5$ MK for the protons, and perhaps as high as 100 MK for minor ion species like oxygen. The fact that such proton/ion temperatures are much higher than the ca. 2 MK inferred for electrons shows clearly that electron heat conduction does not play much role in extending the effect of coronal heating outward in such regions. The fundamental reasons for the differing temperature components are a topic of much current research; one promising model invokes ion cyclotron resonance damping of magnetohydrodynamics waves (Cranmer 2000, 2009).

4.4 Relation to Winds from other Cool Stars

4.4.1 Coronal Winds of Cool Main-Sequence Stars

Like the sun, other cool stars with surface temperatures $T \lesssim 10,000$ low enough for hydrogen recombination are expected to have vigorous subsurface convection zones that generate a strong upward flux of mechanical energy. For *main-sequence* stars in which gravitational stratification implies a sharp, exponential drop in surface density over small-scale height $H \ll R$, this should lead to the same kind of thermal runaway as in the sun (► Sect. 4.1; ► Fig. 15-7), generating a hot corona, and so also an associated, pressure-driven coronal wind expansion. As

noted in [Sect. 2.1](#), observations of X-ray emission and high-ionization UV lines do indeed provide strong evidence for such stellar coronae, but the low density of the very low mass loss rate means there are few direct diagnostics of actual outflow in stellar coronal winds.

4.4.2 Alfvén Wave Pressure Driving of Cool-Giant Winds

By contrast, cool *giants* do show much direct evidence for quite dense, cool winds, without any indication of a hot corona that could sustain a gas-pressure-driven expansion. However, the mechanical energy flux density needed to drive such winds is actually quite comparable to what is inferred for the solar surface, $F_E \approx 10^5 \text{ erg/cm}^2/\text{s}$, which likely could again be readily supplied by their H-recombination convection zones. But a key difference now is that, owing to the much weaker gravitational stratification, this need no longer lead to a thermal runaway.

In particular, consider again the general scaling of the ratio of the gravitational scale height to stellar radius (cf. [15.24](#)),

$$\frac{H}{R} = \frac{2a^2}{v_e^2} = \frac{kTR}{G\mu M} = 4 \times 10^{-4} \frac{(T/T_\odot)(R/R_\odot)}{M/M_\odot}. \quad (15.52)$$

In cool, solar-mass giant stars, the much larger radius can increase the surface value of this ratio by a factor hundred or more over its (very small) solar value, that is, to several percent. Moreover, at the >1 MK coronal temperature of a thermal runaway, the ratio would now be well above unity, instead of ca. 10% found for the solar corona. This would formally put the critical/sonic radius *below* the stellar radius, representing a kind of free expansion of the coronal base, at a supersonic speed well above the surface escape speed, instead of critical transition from subsonic to supersonic outflow. It seems unlikely thermal runaway could be sustained in such an expanding vs. static medium.

But in lieu of runaway heating, it seems instead that the upward mechanical energy flux could readily provide the direct *momentum* addition to drive a relatively slow wind outflow against the much weaker stellar gravity, operating now via a gradient in the pressure associated with *waves* instead of the gas. In general, the mechanical stress or pressure exerted by waves scales, like gas pressure, with the gas density ρ ; but now this is multiplied by the square of a wave velocity amplitude δv , instead of the sound speed a , that is, $P_w = \rho \delta v^2$.

Although the details of how such a wave pressure is generated and evolves depend on the specific type of wave, a general energetic requirement for any waves to be effective in driving a wind outflow is that the fluctuating velocity δv must become comparable to the local gravitational escape speed somewhere near the stellar surface. This already effectively rules out wind driving by sound waves, because to avoid strong damping as shocks, their velocity amplitude must remain subsonic, $\delta v < a$; this implies $P_w < P_{gas}$, and thus that sound waves would be even less effective than gas pressure in driving such cool winds (Koninx and Pijpers 1992).

In this respect, the prospects are much more favorable for magnetohydrodynamic waves, particularly the Alfvén mode. For the simple case of a radially oriented stellar magnetic field $\mathbf{B} = B\hat{r}$, the mean field can impart no outward force to propel a radial wind. But Alfvén wave fluctuations δB *transverse* to the mean field B give the field a wave pressure $P_w = \delta B^2/8\pi$, for which any radial gradient dP_w/dr does have an associated radial force. Moreover, since the fractional amplitude $f = \delta B/B$ of Alfvén waves can be up to order unity, the associated velocity

amplitude δv of these transverse fluctuations can now extend up to the Alfvén speed,

$$v_A \equiv \frac{B}{\sqrt{4\pi\rho}}. \quad (15.53)$$

Unlike for sound waves, this can readily become comparable to the stellar escape speed v_e , implying a ready potential for Alfvén waves to drive a strong stellar wind.

In fact, for Alfvén waves with a fractional amplitude $f = \delta v/v_A = \delta B/B$, requiring $\delta v = v_e = v$ at a wind critical point near the stellar surface radius R gives a direct estimate for the potential wind mass loss rate,

$$\dot{M} \approx \frac{\delta B^2 R^2}{v_e} = 1.2 \times 10^{-7} \frac{M_\odot}{\text{yr}} \frac{\delta B^2 R_{100}^{5/2}}{\sqrt{M/M_\odot}}, \quad (15.54)$$

where $R_{100} \equiv R/(100R_\odot)$ and $\delta B = fB$ is in Gauss. Indeed, note that for the sun, taking $f = 0.1$ and a mean field of one Gauss gives $\dot{M} = 1.2 \times 10^{-14} M_\odot/\text{year}$, which is somewhat fortuitously consistent with the mass flux measured by interplanetary spacecraft (► Sect. 2.1). More significantly, for giant stars with fluctuating fields $\delta B = fB$ of a few Gauss, the scaling in (► 15.54) matches quite well their much higher, observationally inferred mass loss rates. For a wind with this mass loss scaling and terminal speed comparable to the surface escape $v_\infty \approx v_e$, the energy flux density required is

$$F_E = \frac{\dot{M} v_e^2}{4\pi R^2} \approx 5 \times 10^4 \frac{\text{erg}}{\text{cm}^2 \text{s}} f^2 B^2 \sqrt{\frac{M/M_\odot}{R_{100}}}, \quad (15.55)$$

which, as noted above, for typical cool-giant parameters is quite close to solar energy flux density.

Actually, observations indicate such cool-giant winds typically have terminal speeds of only 10–20 km/s, significantly below even their relatively low surface escape speeds $v_e \approx 50$ km/s, and implying that most all (~90%) of the input energy goes toward lifting the wind material out of the star’s gravitational potential. Explaining this together with the large mass loss rate demands a delicate fine-tuning in any wind model, for example that the Alfvén waves are damped over a length scale very near a stellar radius (Hartmann and MacGregor 1980; Holzer et al. 1983). For further details, the reader is referred to the very lucid reviews by Holzer (1987) and Holzer and MacGregor (1985).

4.4.3 Superwind Mass Loss from Asymptotic Giant Branch Stars

Stars with initial mass $M < 8 M_\odot$ are all thought to end up as white dwarfs with mass below the Chandrasekhar limit $M < 1.4 M_\odot$. This requires copious mass loss ($\dot{M} > 10^{-4} M_\odot/\text{year}$) to occur in a relatively brief (~ 10^4 year) “superwind” phase at the end of a star’s evolution on the Asymptotic Giant Branch (AGB). It seems unlikely that mere wave pressure generated in near-surface convection zones could drive such enormous mass loss, and so instead, models have emphasized tapping the more deep-seated driving associated with global stellar *pulsations*. The most effective seem to be the radial pressure or p-modes thought to be excited by the so-called kappa mechanism (Hansen et al. 2004) within interior ionizations zones (e.g., of Helium). Because of the much higher interior temperature and sound speed, such pulsations can have much higher velocity amplitude than surface sound waves. Indeed, as the pulsations propagate

upward through the declining density, their velocity amplitude can increase, effectively lifting gas parcels near the surface a substantial fraction of the stellar radius.

If the subsequent infall phase of these near-surface parcels meets with the next outward pulsation before returning to its previous minimum radius, the net effect is a gradual lifting of material out of the much weakened gravitational potential. Moreover, as the gas cools through the expansion into ever larger radii and away from the stellar photosphere, dust can form, at which point the additional driving associated with scattering and absorption of the bright stellar radiation can propel the coupled medium of gas and dust to full escape from the star. But such dust-driving is only possible when the pulsations are able to effectively “levitate” stellar material in a much weakened gravity.

As reviewed by Willson (2000), models suggest the net mass loss can eventually become so effective that the associated mass loss timescale $\tau_M = M/\dot{M}$ becomes shorter than the timescale for interior evolution, representing then a kind of “death line” at which the entire stellar envelope is effectively lost, leaving behind only the hot, dense, degenerate stellar core to become a white dwarf remnant. Overall, this process seems arguably a largely interior evolution issue, more akin to a “critical overflow” (e.g., like the “Roche lobe” overflow in mass exchange binaries) than a steady, supersonic outflow from a fixed stellar surface. As such, the kind of simplified steady-state wind formalism outlined here is perhaps of limited relevance. The reader is thus referred to the review by Willson (2000) and references therein for a more detailed discussion of this extreme final stage of cool-star mass loss.

4.5 Summary for the Solar Wind

- The solar wind is driven by the gas-pressure gradient of the high-temperature solar corona.
- The hot corona is the natural consequence of heating from mechanical energy generated in the solar convection zone. At low density radiative cooling cannot balance this heating, leading to a thermal runaway up to temperatures in excess of a million degrees, at which inward thermal conduction back into the atmosphere can again balance the heating.
- Outward thermal conduction can extend this high temperature well away from the coronal base.
- For such a hot, extended corona, hydrostatic stratification would lead to an asymptotic pressure that exceeds the interstellar value, thus requiring a net outward coronal expansion that becomes the supersonic solar wind.
- Because the wind mass flux is a sensitive function of the coronal temperature, the energy loss from wind expansion acts as an effective coronal thermostat.
- While the mass loss rate is thus set by energy deposition in the subsonic wind base, energy added to the supersonic region increases the flow speed.
- The high-speed wind streams that emanate from coronal holes require extended energy deposition. Coronal-hole observations showing the proton temperature significantly exceeds the electron temperature rule out electron heat conduction as the mechanism for providing the extended energy.
- Magnetic fields lead to extensive structure and variability in the solar corona and wind.
- Other cool main-sequence stars likely also have hot, pressure-driven coronal winds, but the dense, cool winds of cool giants could instead be driven by the pressure from Alfvén waves.

5 Radiatively Driven Winds from Hot, Massive Stars

Among the most massive stars – which tend also to be the hottest and most luminous – stellar winds can be very strong, with important consequences for both the star’s own evolution, and for the surrounding interstellar medium. In contrast to the *gas*-pressure-driven solar wind, such hot-star winds are understood to be driven by the pressure gradient of the star’s emitted *radiation*.

The sun is a relatively low-mass, cool star with a surface temperature about 6,000 K; but as discussed above, its wind arises from pressure-expansion of the very hot, million-degree solar corona, which is somehow superheated by the mechanical energy generated from convection in the sun’s subsurface layers. By contrast, high-mass stars with much hotter surface temperatures (10,000–100,000 K) are thought to lack the strong convection zone needed to heat a circum-stellar corona; their stellar winds thus remain at temperatures comparable to the star’s surface, and so lack the very high gas pressure needed to drive an outward expansion against the stellar gravity.

However, such hot stars have a quite high radiative flux, since by the Stefan–Boltzmann law this scales as the fourth power of the surface temperature. Because light carries momentum as well as energy, this radiative flux imparts a force to the atoms that scatter the light. At the level of the star’s atmosphere where this force exceeds the inward force of the stellar gravity, material is accelerated upward and becomes the stellar wind.

An important aspect of this radiative driving process is that it often stems mostly from *line* scattering. As discussed in [Sect. 2.2](#), in a static medium such line interactions are confined to radiation wavelengths within a narrow thermal width of line center. However, in an accelerating stellar wind flow, the Doppler effect shifts the resonance to increasingly longer wavelengths, allowing the line scattering to sweep gradually through a much broader portion of the stellar spectrum (see [Fig. 15-3](#)). This gives the dynamics of such winds an intricate feedback character, in which the radiative driving force that accelerates the stellar wind depends itself on that acceleration.

5.1 Radiative Acceleration

5.1.1 Electron Scattering and the Eddington Limit

Before analyzing the radiative acceleration from line scattering, let us first consider the simpler case of scattering by free electrons, which is a “gray,” or frequency-independent process. Since gray scattering cannot alter the star’s total luminosity L , the radiative energy flux at any radius r is simply given by $F = L/4\pi r^2$, corresponding to a radiative *momentum* flux of $F/c = L/4\pi r^2 c$. As noted in [Sect. 2.2.1](#), the opacity for electron scattering is $\kappa_e = 0.2(1 + X) = 0.34 \text{ cm}^2/\text{g}$, where the latter result applies for the standard (solar) hydrogen mass fraction $X = 0.72$. The product of this opacity and the radiative momentum flux yields the radiative acceleration (force-per-unit-mass) from free-electron scattering,

$$g_e(r) = \frac{\kappa_e L}{4\pi r^2 c}. \quad (15.56)$$

It is of interest to compare this with the star’s gravitational acceleration, GM/r^2 . Since both accelerations have the same $1/r^2$ dependence on radius, their ratio is spatially constant, fixed by

the ratio of luminosity to mass,

$$\Gamma_e = \frac{\kappa_e L}{4\pi GMc}. \quad (15.57)$$

This ratio, sometimes called the Eddington parameter, thus has a characteristic value for each star. For the sun it is very small, of order 2×10^{-5} , but for hot, massive stars it can approach unity. As noted by Eddington, electron scattering represents a basal radiative acceleration that effectively counteracts the stellar gravity. The limit $\Gamma_e \rightarrow 1$ is known as the Eddington limit, for which the star would become gravitationally unbound.

It is certainly significant that hot stars with strong stellar winds have Γ_e only a factor two or so below this limit, since it suggests that only a modest additional opacity could succeed in fully overcoming gravity to drive an outflow. But it is important to realize that a stellar wind represents the outer envelope outflow from a nearly static, gravitationally bound base, and as such is not consistent with an *entire* star exceeding the Eddington limit. Rather the key requirement for a wind is that the driving force increases naturally from being smaller to larger than gravity at some radius near the stellar surface. How the force from line-scattering is ideally suited for just such a spatial modulation is described next.

5.1.2 Driving By Doppler-Shifted Resonant Line Scattering

As discussed in [Sect. 2.2](#), the *resonant strength* and sensitive *wavelength dependence* of bound-bound *line* opacity leads to strong, characteristic interactions of stellar radiation with the expanding wind material, giving rise to distinct features in the emergent stellar spectrum, like asymmetric P-Cygni line profiles, which provide key signatures of the wind expansion. These same basic properties – resonance strength and Doppler shift of the line resonance in the expanding outflow – also make the radiative force from line scattering the key factor in driving most massive-star winds. Relative to free-electron scattering, the overall amplification factor for a broadband, untuned radiation source is set by the *quality* of the resonance, $Q \approx \nu_0/A$, where ν_0 is the line frequency and A is decay rate of the excited state. For quantum mechanically allowed atomic transitions, this can be very large, of order 10^7 . Thus, even though only a very small fraction ($\sim 10^{-4}$) of electrons in a hot-star atmosphere are bound into atoms, illumination of these atoms by an *unattenuated* (i.e., optically thin), broadband radiation source would yield a collective line-force which exceeds that from free electrons by about a factor $\bar{Q} \approx 10^7 \times 10^{-4} = 1,000$ (Gayley 1995). For stars within a factor two of the free-electron Eddington limit, this implies that line scattering is capable, in principle, of driving material outward with an acceleration on order a *thousand* times the inward acceleration of gravity!

In practice, of course, this does not normally occur, since any sufficiently large collection of atoms scattering in this way would readily block the limited flux available within just the narrow frequency bands tuned to the lines. Indeed, in the static portion of the atmosphere, the flux is greatly reduced at the line frequencies. Such line “saturation” keeps the overall line force quite small, in fact well below the gravitational force, which thus allows the inner parts of the atmosphere to remain gravitationally bound.

This, however, is where the second key factor, the *Doppler effect*, comes into play. As illustrated in [Fig. 15-3](#), in the outward-moving portions of the outer atmosphere, the Doppler effect redshifts the local line resonance, effectively desaturating the lines by allowing the atoms to resonate with relatively unattenuated stellar flux that was initially at slightly higher frequencies. By effectively sweeping a broader range of the stellar flux spectrum, this makes it possible

for the line force to overcome gravity and accelerate the very outflow it itself requires. As quantified within the CAK wind theory described below, the amount of mass accelerated adjusts such that the self-absorption of the radiation reduces the overall line-driving to being just somewhat (not a factor thousand) above what is needed to overcome gravity.

5.1.3 Radiative Acceleration from a Single, Isolated Line

For weak lines that are optically thin in the wind (i.e., with a characteristic optical depth from [☛ 15.5], $\tau_o \ll 1$), the line-acceleration takes a form similar to the simple electron scattering case (cf. [☛ 15.56]),

$$g_{thin} \equiv \frac{\kappa v_{th} v_o L_v}{4\pi r^2 c^2} = w_{v_o} q g_e, \quad (15.58)$$

where κ characterizes the opacity near line center, $q \equiv \kappa v_{th} / \kappa_e c$ is a dimensionless measure of the frequency-integrated line opacity (cf. [☛ Sect. 2.2.2]), and $w_{v_o} \equiv v_o L_v / L$ weights the placement of the line within the luminosity spectrum L_v .

For stronger lines, the absorption and scattering of radiation can be treated within the Sobolev approximation in terms of the optical thickness of the *local* Sobolev resonance zone, as given in [☛ Sect. 2.2 for nonradial rays integrated over the finite-size star (see [☛ 15.7–15.9]). In the further approximation of purely radial streaming radiation from a point-like star, the radial acceleration takes the form,

$$g_{line} \approx g_{thin} \frac{1 - e^{-\tau_{Sob}}}{\tau_{Sob}}. \quad (15.59)$$

wherein the reduction from the optically thin case depends only on the local radial Sobolev optical depth given in [☛ 15.3], which is rewritten here as

$$\tau_{Sob} = \rho \kappa l_{Sob} = \frac{\rho \kappa v_{th}}{dv/dr} = \frac{\rho q \kappa_e c}{dv/dr} \equiv qt. \quad (15.60)$$

In the final equality, $t \equiv \kappa_e \rho c / (dv/dr)$ is the Sobolev optical depth for a line with integrated strength equal to free-electron scattering, that is, with $q = 1$.

In the limit of a very optically thick line with $\tau_s \gg 1$, the acceleration becomes,

$$g_{thick} \approx \frac{g_{thin}}{\tau_s} = w_{v_o} \frac{L}{4\pi r^2 \rho c^2} \frac{dv}{dr} = w_{v_o} \frac{L}{M c^2} v \frac{dv}{dr}, \quad (15.61)$$

where the last equality uses the definition of the wind mass loss rate, $\dot{M} \equiv 4\pi \rho v r^2$. A key result here is that the optically thick line force is *independent* of the line strength q , and instead varies in proportion to the velocity gradient dv/dr . The basis of this is illustrated by [☛ Fig. 15-3, which shows that the local *rate* at which stellar radiation is redshifted into a line resonance depends on the *slope* of the velocity. By Newton's famous equation of motion, a force is normally understood to *cause* an acceleration. But here it is seen that an optically thick line-force also *depends* on the wind's advective rate of acceleration, $v dv/dr$.

5.1.4 Sobolev Localization of Line-Force Integrals for a Point Star

To provide a more quantitative illustration of this Sobolev approximation, let us now derive these key properties of line-driving through the localization of the spatial optical depth integral.

Under the simplifying approximation that the stellar radiation flux is purely radial (as from a central point-source), the force-per-unit-mass associated with direct absorption by a single line at a radius r is given by

$$g_{line}(r) = g_{thin} \int_{-\infty}^{\infty} dx \phi(x - u(r)) e^{-\tau(x,r)}. \quad (15.62)$$

The integration is over a scaled frequency $x \equiv (v/v_o - 1)(c/v_{th})$, defined from line center in units of the frequency broadening associated with the ion thermal speed v_{th} , and $u(r) \equiv v(r)/v_{th}$ is the radial flow speed in thermal-speed units. The integrand is weighted by the line profile function $\phi(x)$, which for thermal broadening typically has the Gaussian form $\phi(x) \sim e^{-x^2}$. The exponential reduction takes account of absorption, as set by the frequency-dependent optical depth to the stellar surface radius R ,

$$\tau(x, r) \equiv \int_R^r dr' \kappa \rho(r') \phi(x - u(r')). \quad (15.63)$$

A crucial point in evaluating this integral is that in a supersonic wind, the variation of the integrand is dominated by the velocity variation within the line-profile. As noted above, this variation has a scale given by the Sobolev length $l_{Sob} \equiv v_{th}/(dv/dr)$, which is smaller by a factor v_{th}/v than the competing density/velocity scale, $H \equiv |\rho/(d\rho/dr)| \approx v/(dv/dr)$. A key step in the Sobolev approximation is thus to recast this spatial integration as an integration over the comoving-frame frequency $x' \equiv x - u(r')$,

$$\tau(x, r) = - \int_{x'(R)}^{x'(r)} \frac{dx' v_{th}}{dv/dr'} \kappa \rho(x') \phi(x') \approx \tau_{Sob} \Phi(x - u(r)), \quad (15.64)$$

where the integrated profile

$$\Phi(x) \equiv \int_x^{\infty} dx' \phi(x'), \quad (15.65)$$

and the latter approximation in (15.64) uses the assumption that $v(r) \gg v_{th}$ to formally extend the surface frequency $x'(R)$ to infinity relative to the local resonance $x'(r)$. As defined in (15.60), the Sobolev optical thickness $\tau_s = qt$ arises here as a collection of spatial variables that are assumed to be nearly constant over the Sobolev resonance zone, and thus can be extracted outside the integral.

Finally, a remarkable, extra bonus from this approximation is that the resulting optical depth (15.64) now has precisely the form needed to allow analytic evaluation of the line-force integral (15.62), yielding directly the general Sobolev force expression given in (15.59).

5.2 The CAK Model for Line-Driven Winds

5.2.1 The CAK Line-Ensemble Force

In practice, a large number of lines with a range of frequencies and strengths can contribute to the wind driving. Castor et al. (1975; hereafter CAK) introduced a practical formalism for computing the cumulative line-acceleration from a parameterized line-ensemble, under the simplifying assumption that the spectral distribution keeps the individual lines nearly independent.

For the point-star model used above, direct summation of the individual line-accelerations as given by (15.59) yields

$$g_{tot} = g_e \sum w_{v_o} q \frac{1 - e^{-qt}}{qt} \approx g_e \int_0^\infty q \frac{dN}{dq} \frac{1 - e^{-qt}}{qt} dq, \quad (15.66)$$

where the latter equality approximates the discrete sum as a continuous integral over the flux-weighted number distribution dN/dq . Following CAK, a key further simplification is to approximate this number distribution as a simple power law in the line strength q ,

$$q \frac{dN}{dq} = \frac{1}{\Gamma(\alpha)} \left(\frac{q}{\bar{Q}} \right)^{\alpha-1}, \quad (15.67)$$

where $\Gamma(\alpha)$ is the complete Gamma function, the CAK power-law index satisfies $0 < \alpha < 1$, and the above mentioned cumulative line strength \bar{Q} provides a convenient overall normalization (cf. Sect. 4.2.2). Application of (15.67) in (15.66) then yields the CAK, point-star, radiative acceleration from this line-ensemble,

$$\begin{aligned} g_{CAK} &= \frac{\bar{Q}^{1-\alpha}}{(1-\alpha)} \frac{g_e}{t^\alpha} \\ &= \frac{1}{(1-\alpha)} \frac{\kappa_e L \bar{Q}}{4\pi r^2 c} \left(\frac{dv/dr}{\rho c \bar{Q} \kappa_e} \right)^\alpha. \end{aligned} \quad (15.68)$$

Note that this represents a kind of “geometric mean” between the optically thin and thick forms (15.58) and (15.61) for a single line.²

5.2.2 CAK Dynamical Solution for Mass Loss Rate and Terminal Speed

The simple, local CAK/Sobolev expression (15.68) for the cumulative line-driving force in the point-star approximation provides a convenient basis for deriving the basic scalings for a line-driven stellar wind. Since, as noted above, the gas pressure is not of much importance in the overall wind driving, let us just consider the steady-state equation of motion (15.31) in the limit of zero sound speed, $a = 0$. This simply requires that the wind acceleration must equal the line-acceleration minus the inward acceleration of gravity,

$$v \frac{dv}{dr} = g_{CAK} - \frac{GM(1-\Gamma_e)}{r^2}, \quad (15.69)$$

wherein we have also taken into account the effective reduction of gravity by the free-electron scattering factor Γ_e . Note from (15.68) that the CAK line-force g_{CAK} depends itself on the flow acceleration it drives.

²CAK dubbed the ratio g_{CAK}/g_e the “force multiplier,” written as $M(t) = kt^{-\alpha}$, with k a normalization constant. Note however that their original formulation used a fiducial thermal speed v_{th} in the definition of the optical depth parameter $t = \kappa_e \rho v_{th} / (dv/dr)$, which then gives an artificial thermal speed dependence to the CAK normalization, $k = (v_{th}/c)^\alpha \bar{Q}^{1-\alpha} / (1-\alpha)$. In the Sobolev approximation, the line-force has no physical dependence on the thermal-speed, and so the formal inclusion of a fiducial v_{th} in the CAK parameterization has sometimes led to confusion, e.g., in applying tabulations of the multiplier constant k . The formulation here avoids this problem, since the parameters q , \bar{Q} , and $t = \kappa_e \rho c / (dv/dr)$ are all independent of v_{th} . A further advantage is that, for a wide range of hot-star parameters, the line normalization has a relatively constant value $\bar{Q} \approx 2000Z$, where Z is the metallicity relative to the standard solar value (Gayley 1995).

Since this feedback between line-driving and flow acceleration is moderated by gravity, let us define the gravitationally scaled inertial acceleration,

$$w' \equiv \frac{r^2 v v'}{GM(1 - \Gamma_e)}. \quad (15.70)$$

In terms of an inverse-radius coordinate $x \equiv 1 - R/r$, note that $w' = dw/dx$, where $w \equiv v^2/v_{esc}^2(1 - \Gamma_e)$ represents the ratio of wind kinetic energy to the (electron-force-reduced) effective gravitational binding from the surface. Using (15.68), the equation of motion can then be rewritten in the simple, dimensionless form,

$$w' = C w'^{\alpha} - 1, \quad (15.71)$$

where the constant is given by

$$C = \frac{1}{1 - \alpha} \left(\frac{\bar{Q}\Gamma_e}{1 - \Gamma_e} \right)^{1-\alpha} \left(\frac{L}{Mc^2} \right)^{\alpha}. \quad (15.72)$$

Figure 15-9 illustrates the graphical solution of this dimensionless equation of motion for various values of the constant C . For fixed stellar and opacity-distribution parameters, this corresponds to assuming various values of the mass loss rate \dot{M} , since $C \propto 1/\dot{M}^{\alpha}$. For high \dot{M} (low C), there are no solutions, while for low \dot{M} (high C), there are two solutions. The two limits are separated by a critical case with one solution – corresponding to the maximal mass loss rate – for which the function Cw'^{α} intersects the line $1 + w'$ at a tangent.

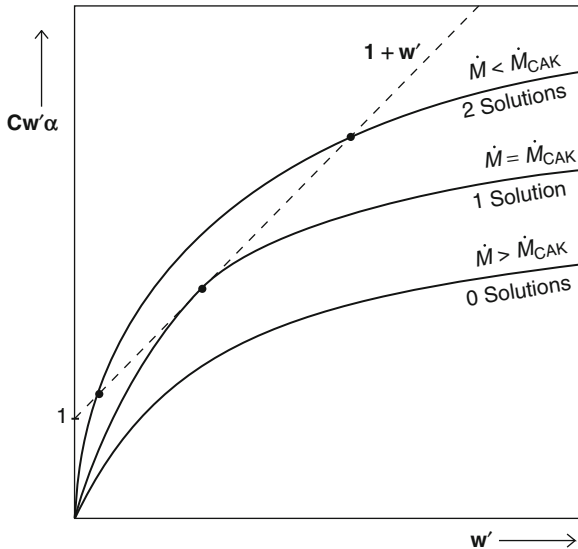


Fig. 15-9

Graphical solution of the dimensionless equation of motion (15.71) representing a 1D, point-star, zero-sound-speed CAK wind, as controlled by the constant $C \sim 1/\dot{M}^{\alpha}$. If \dot{M} is too big, there are no solutions; if \dot{M} is small there are two solutions. A maximal value $\dot{M} = \dot{M}_{CAK}$ defines a single, “critical” solution

the tangency requirement implies $\alpha C_c w_c^{\alpha-1} = 1$, which together with the original (► 15.71) yields the critical conditions $w_c' = \alpha/1 - \alpha$ and $C_c = 1/\alpha^\alpha (1 - \alpha)^{1-\alpha}$.

From (► 15.72), this critical value of C_c defines the maximal CAK mass loss rate

$$\dot{M}_{CAK} = \frac{L}{c^2} \frac{\alpha}{1 - \alpha} \left[\frac{\bar{Q}\Gamma_e}{1 - \Gamma_e} \right]^{(1-\alpha)/\alpha}. \quad (15.73)$$

Moreover, since (► 15.71) has no explicit spatial dependence, these critical conditions hold at all radii. By spatial integration of the critical acceleration w_c' from the surface radius R , we thus obtain a specific case of the general “beta”-velocity law,

$$v(r) = v_\infty \left(1 - \frac{R_*}{r} \right)^\beta, \quad (15.74)$$

where $\beta = 1/2$, and the wind terminal speed $v_\infty = v_{esc} \sqrt{\alpha(1 - \Gamma_e)/(1 - \alpha)}$.

An important success of these CAK scaling laws is the theoretical rationale they provide for an empirically observed “wind momentum–luminosity” (WML) relation (Kudritzki et al. 1995). Combining the CAK mass-loss law (► 15.73) together with the scaling of the terminal speed with the effective escape, we obtain a WML relation of the form,

$$\dot{M} v_\infty \sqrt{R_*} \sim L^{1/\alpha} \bar{Q}^{-1/\alpha-1} \quad (15.75)$$

wherein we have neglected a residual dependence on $M(1 - \Gamma_e)$ that is generally very weak for the usual case that α is near $2/3$. Fits for galactic OB supergiants (Puls et al. 1996) give a luminosity slope consistent with $\alpha \approx 0.6$, with a normalization consistent with $\bar{Q} \approx 10^3$. Note that the direct dependence $\bar{Q} \sim Z$ provides the scaling of the WML with metallicity Z .

5.3 Extensions of Idealized CAK Model

5.3.1 Finite-Size Star

These CAK results strictly apply only under the idealized assumption that the stellar radiation is radially streaming from a point-source. If one takes into account the finite angular extent of the stellar disk, then near the stellar surface the radiative force is reduced by a factor $f_{d*} \approx 1/(1 + \alpha)$, leading to a reduced mass loss rate (Friend and Abbott 1986; Pauldrach et al. 1986),

$$\dot{M}_{fd} = f_{d*}^{1/\alpha} \dot{M}_{CAK} = \frac{\dot{M}_{CAK}}{(1 + \alpha)^{1/\alpha}} \approx \dot{M}_{CAK}/2. \quad (15.76)$$

Away from the star, the correction factor increases back toward unity, which for the reduced base mass flux implies a stronger, more extended acceleration, giving a somewhat higher terminal speed, $v_\infty \approx 3v_{esc}$, and a flatter velocity law, approximated by replacing the exponent in (► 15.74) by $\beta \approx 0.8$.

5.3.2 Radial Variations in Ionization

The effect of a radial change in ionization can be approximately taken into account by correcting the CAK force (► 15.68) by a factor of the form $(n_e/W)^\delta$, where n_e is the electron density,

$W \equiv 0.5(1 - \sqrt{1 - R_*/r})$ is the radiation “dilution factor,” and the exponent has a typical value $\delta \approx 0.1$ (Abbott 1982). This factor introduces an additional density dependence to that already implied by the optical depth factor $1/t^\alpha$ given in (► 15.68). Its overall effect can be roughly taken into account with the simple substitution $\alpha \rightarrow \alpha' \equiv \alpha - \delta$ in the power exponents of the CAK mass loss scaling law (► 15.73). The general tendency is to moderately increase \dot{M} , and accordingly to somewhat decrease the wind speed.

5.3.3 Finite Gas Pressure and Sound Speed

The above scalings also ignore the finite gas pressure associated with a small but nonzero sound speed a . If we apply the full gas-pressure equation of motion (► 15.31) to the case with line-driving ($g_x = g_{CAK}$), then through a perturbation expansion in the small parameter a/v_{esc} , it is possible to derive simple scalings for the fractional corrections to the mass loss rate and terminal speed (Owocki and ud-Doula 2004),

$$\delta m \approx \frac{4\sqrt{1-\alpha}}{\alpha} \frac{a}{v_{esc}}; \quad \delta v_\infty \approx \frac{-\alpha \delta m}{2(1-\alpha)} \approx \frac{-2}{\sqrt{1-\alpha}} \frac{a}{v_{esc}}. \quad (15.77)$$

For a typical case with $\alpha \approx 2/3$ and $a \approx 20 \text{ km/s} \approx v_{esc}/30$, the net effect is to increase the mass loss rate and decrease the wind terminal speed, both by about 10%.

5.4 Wind Instability and Variability

The steady, spherically symmetric, line-driven-wind models described above have had considerable success in explaining the inferred general properties of OB-star winds, like the total mass loss rate and mean velocity law. But when viewed more carefully there is substantial evidence that such winds are actually quite highly structured and variable on a broad range of spatial and temporal scales.

Large-scale variations give rise to *Discrete Absorption Components* (DACs) seen in UV spectra lines (Howarth and Prinja 1989; Fullerton 2003). These begin as broad absorption enhancement in the inner part of the blue absorption trough of an unsaturated P-Cygni line, which then gradually narrow as they drift, over a period of days, toward the blue-edge of the profile. These DACs likely result from disturbances (e.g., localized magnetic fields or nonradial pulsations) at the photospheric base of the stellar wind, which through stellar rotation evolve in the wind into semi-regular “Co-rotating Interaction Regions” (CIRs: Mullan 1984; Cranmer and Owocki 1996), much as detected directly in the solar wind at boundaries between fast and slow wind streams (see ► Sect. 2.1).

But there is also strong, though indirect evidence that OB winds have an extensive, small-scale, turbulent structure. Saturated P-Cygni lines have extended black troughs thought to be a signature that the wind velocity is highly nonmonotonic (Lucy 1982), and such stars commonly exhibit soft X-ray emission thought to originate from embedded wind shocks (Cohen 2008).

This small-scale flow structure likely results from the strong *Line-Des shadowing Instability* (LDI) that is intrinsic to the radiative driving by line scattering (MacGregor et al. 1979; Owocki and Rybicki 1984, 1985). As noted above, there is a strong hidden potential in line scattering to drive wind material with accelerations that greatly exceed the mean outward acceleration. For any small velocity perturbations with a length scale near or below the Sobolev length l_{Sob} ,

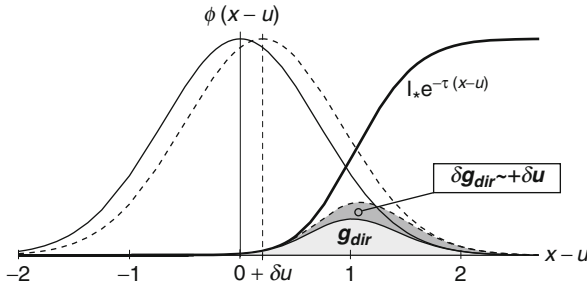


Fig. 15-10

Illustration of the physical origin of the line deshadowing instability. At an arbitrary point in the expanding wind, it shows the line profile ϕ and direct intensity from the star plotted vs. comoving-frame frequency $x - u$. The light shaded overlap area is proportional to the component line-acceleration g_{dir} . The dashed profile shows the effect of the Doppler shift from a perturbed velocity δu (in units of thermal speed v_{th}), with the resulting extra area in the overlap with the blue-edge intensity giving a perturbed line-force δg that scales in proportion to this perturbed velocity

linear stability analyses show that the perturbed radiative acceleration δg no longer scales with the velocity gradient $\delta v'$, as expected from the above Sobolev analysis (Abbott 1980), but rather in direct proportion to the perturbed velocity itself, $\delta g \sim \delta v$ (MacGregor et al. 1979; Owocki and Rybicki 1984). This leads to a strong instability, in which the stronger acceleration leads to a faster flow, which in turns leads to an even stronger acceleration (see Fig. 15-10).

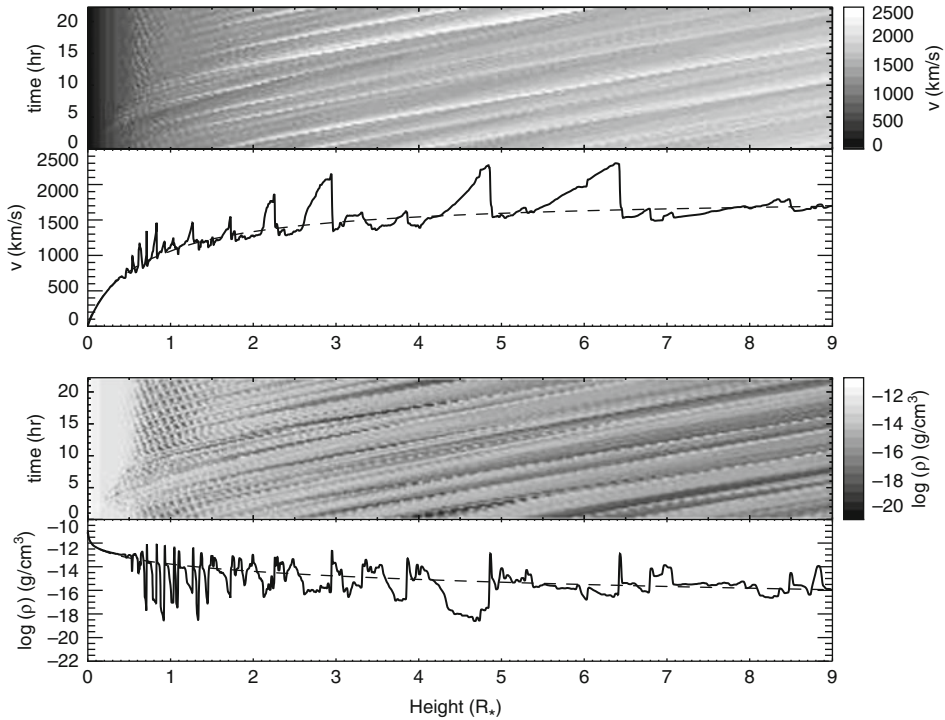
The growth rate of this instability scales with the ratio of the mean driving force to the ion thermal speed, $\omega_g \approx g_{CAK}/v_{th}$. Since the CAK line-driving also sets the flow acceleration, that is, $g_{CAK} \approx v dv/dr$, it is readily found that the growth is approximately at the flow rate through the Sobolev length, $\omega_g \approx v/l_{Sob}$. This is a large factor $v/v_{th} \approx 100$ bigger than the typical wind expansion rate $dv/dr \approx v/R$, implying then that a small perturbation at the wind base would, within this lineary theory, be amplified by an enormous factor, of order $e^{v/v_{th}} \approx e^{100}$!

In practice, a kind of “line-drag” effect of the *diffuse* component of radiation scattered within the lines reduces this stability (Lucy 1984; Owocki and Rybicki 1985), giving a net growth rate that scales roughly as

$$\omega_g(r) \approx \frac{g_{CAK}}{v_{th}} \frac{\mu_*(r)}{1 + \mu_*(r)}, \quad (15.78)$$

where $\mu_* \equiv \sqrt{1 - R^2/r^2}$. This net growth rate vanishes near the stellar surface, where $\mu_* = 0$, but it approaches half the pure-absorption rate far from the star, where $\mu_* \rightarrow 1$. This implies that the outer wind is still very unstable, with cumulative growth of ca. $v_\infty/2v_{th} \approx 50$ e-folds.

Because the instability occurs at spatial scales near and below the Sobolev length, hydrodynamical simulations of its nonlinear evolution cannot use the Sobolev approximation, but must instead carry out *nonlocal* integrals for both direct and diffuse components of the line radiation transport (Owocki et al. 1988; Feldmeier 1995; Owocki and Puls 1996, 1999). The right panel of Fig. 15-11 illustrates typical results of a 1-D time-dependent simulation. Because of the stabilization from line-drag, the flow near the photospheric wind base follows the steady, smooth CAK form (dashed curve), but beginning about $r \approx 1.5R$, the strong intrinsic instability lead to extensive wind structure, characterized by high-speed rarefactions in between slower dense, compressed shells.



■ Fig. 15-11

Results of 1-D, time-dependent numerical hydrodynamics simulation of the nonlinear growth of the instability. The line plots show the spatial variation of velocity (*upper*) and density (*lower*) at a fixed, arbitrary time snapshot. The corresponding gray scales show both the time (*vertical axis*) and height (*horizontal axis*) evolution. The dashed curve shows the corresponding smooth, steady CAK model, from the vertical in intervals of 4,000 s from the CAK initial condition

Because of the computational expense of carrying out the nonlocal integrals for the line-acceleration, 2-D simulations of this instability have so far been limited, either ignoring or using simplified approximations for the lateral components of the diffuse line-drag (Owocki 1999; Dessart and Owocki 2003, 2005). But results so far indicate the compressed shells of 1-D simulations should break up into small-scale clumps, with a characteristic size of a few percent of the local radius, and a volume filling factor $f_v \approx 0.1$. As noted in ► Sect. 2.2.1, this has important implications for interpreting diagnostics that scale with the square of wind density, suggesting that mass loss rates based on such diagnostics may need to be reduced by factors of a few, that is, $1/\sqrt{f_v} \approx \sqrt{10}$.

5.5 Effect of Rotation

The hot, luminous stars that give rise to line-driven stellar winds tend generally to have quite rapid stellar rotation. This is most directly evident through the extensive broadening of their

photospheric absorption lines, which suggest projected equatorial rotation speeds $V_{rot} \sin i$ of hundreds of km/s, where $\sin i \leq 1$ accounts for the inclination angle i of the observer line of sight to the stellar rotation axis. In some of the most rapid rotators, e.g., the Be stars, the surface rotation speed V_{rot} is inferred to be a substantial fraction, perhaps 70–80% or more, of the so-called critical rotation speed, $V_{crit} \equiv \sqrt{2GM/R}$, for which material at the equatorial surface would be in Keplerian orbit (Townsend et al. 2004).

Initial investigations (Friend and Abbott 1986; Pauldrach et al. 1986) of the effect of rotation on radiatively driven winds derived 1-D models based on the standard CAK line-driving formalism, but now adding the effect of a centrifugally reduced, *effective* surface gravity as a function of colatitude θ ,

$$g_{eff}(\theta) = \frac{GM}{R^2} (1 - \Omega^2 \sin^2 \theta), \quad (15.79)$$

where $\Omega^2 \equiv V_{rot}^2 R/GM$, and for simplicity, we have ignored any rotational distortion of the surface radius R . This allows one to write the standard CAK mass loss rate scaling law (cf. [15.73]) in terms of *surface* values of the mass flux $\dot{m} = \rho v$, radiative flux F , and effective gravity g_{eff} , relative to corresponding polar ($\theta = 0$) values \dot{m}_o , F_o , and $g_o = GM/R^2$,

$$\frac{\dot{m}(\theta)}{\dot{m}_o} = \left[\frac{F(\theta)}{F_o} \right]^{1/\alpha} \left[\frac{g_{eff}(\theta)}{g_o} \right]^{1-1/\alpha}. \quad (15.80)$$

If, as was initially assumed, the surface flux is taken to be constant in latitude, $F(\theta) = F_o$, then we obtain the scaling

$$\frac{\dot{m}(\theta)}{\dot{m}_o} = [1 - \Omega^2 \sin^2 \theta]^{1-1/\alpha}; \quad F(\theta) = F_o. \quad (15.81)$$

Since $\alpha < 1$, the exponent $1-1/\alpha$ is negative, implying that the mass flux increases monotonically from pole ($\sin \theta \rightarrow 0$) toward the equator ($\sin \theta \rightarrow 1$).

However, as first demonstrated by von Zeipel (1924), for a radiative stellar envelope undergoing solid body rotation, the emergent radiative flux at any latitude is predicted to vary in proportion to the centrifugally reduced effective gravity, $F(\theta) \sim g_{eff}$. Applying this equatorial “gravity darkening” for the surface flux, we obtain

$$\frac{\dot{m}(\theta)}{\dot{m}_o} = 1 - \Omega^2 \sin^2 \theta; \quad F(\theta) \sim g_{eff}(\theta) \quad (15.82)$$

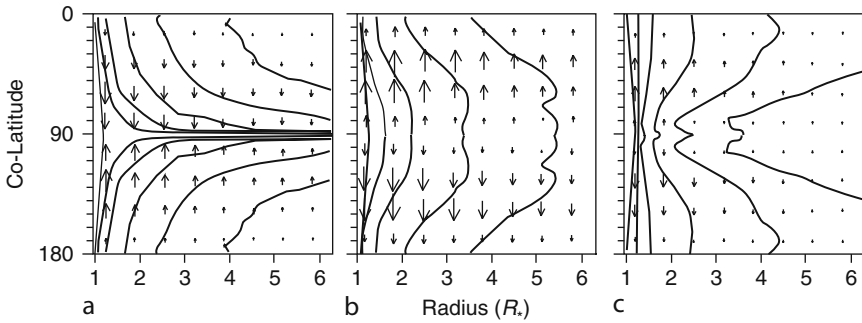
so that the mass flux now *decreases* toward the equator, with a maximum at the *pole*!

Recalling that the wind terminal speed tends to scale with the surface gravity through the escape speed, this 1-D analysis also predicts a latitudinally varying wind speed that is proportional to a centrifugally reduced, effective escape speed,

$$v_\infty(\theta) \sim v_{esc} \sqrt{1 - \Omega^2 \sin^2 \theta}. \quad (15.83)$$

The latitudinal variation of wind density is then obtained from $\rho(\theta) \sim \dot{m}(\theta)/v_\infty(\theta)$.

More generally, the wind from a rotating star can also flow in latitude as well as radius, requiring then a 2-D model. In this regard, a major conceptual advance was the development of the elegantly simple “Wind Compressed Disk” (WCD) paradigm by Bjorkman and Cassinelli (1993). They noted that, like satellites launched into earth orbit, parcels of gas gradually driven radially outward from a rapidly rotating star should remain in a tilted “orbital plane” that brings them over the equator, where they collide to form compressed disk. Initial 2-D hydrodynamical simulations (Owocki et al. 1994) generally confirmed the basic tenets of the WCD model



■ Fig. 15-12

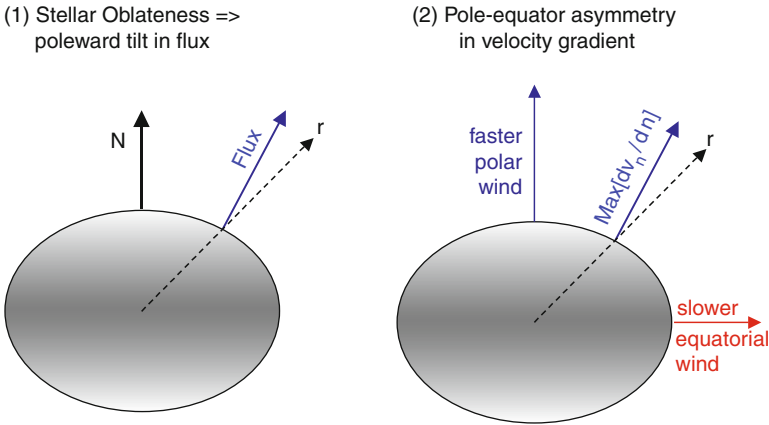
Contours of density in stellar wind from a star rotating at 75% of critical rate, plotted vs. colatitude θ and radius r , spaced logarithmically with two contours per decade. The superposed vectors represent the latitudinal velocity, with the maximum length corresponding to a magnitude of $v_\theta = 100$ km/s. The three panels show the cases (a) without nonradial forces or gravity darkening; (b) with nonradial forces but no gravity darkening, and; (c) with both nonradial forces and gravity darkening

(► Fig. 15-12a), with certain detailed modifications (e.g., infall of inner disk material). But later simulations (Owocki et al. 1996) that account for a net poleward component of the line-driving force (► Fig. 15-13) showed that this can effectively *reverse* the equatorward drift, and so completely *inhibit* formation of any equatorial compressed disk (► Fig. 15-12b). Indeed, when equatorial gravity darkening is taken into account, the lower mass flux from the equator makes the equatorial wind have a reduced, rather than enhanced, density (► Fig. 15-12c).

The net upshot then is that a radiatively driven wind from a rapidly rotating star is predicted to be both faster and denser over the poles, instead of the equator. This may help explain spectroscopic and interferometric evidence that the current-day wind of the extreme massive star η Carinae is faster and denser over the poles, leading to a prolate shape for its dense, optically thick “wind photosphere” (Smith et al. 2003; van Boekel et al. 2003; Groh et al. 2010). Extensions of the rotational scalings to the case of continuum-driven mass loss could also explain the bipolar shape of the Homunculus nebula (Owocki et al. 2004).

5.6 Summary for Radiatively Driven Massive-Star Winds

- The large ratio of luminosity to mass means OB stars are near the “Eddington limit,” for which the radiative force from just scattering by free electrons nearly cancels the stellar gravity.
- The resonance nature of line absorption by bound electrons makes their cumulative effective opacity of order a thousand times larger than free electrons, but the discrete energies of bound states means the opacity is tuned to very specific photon wavelengths.
- In a static atmosphere, saturation of line absorption keeps the associated force smaller than gravity; but in an accelerating wind, the associated Doppler shift of the line frequency exposes it to fresh continuum radiation, allowing the line-force to become strong enough to overcome gravity and drive the outflow.



■ Fig. 15-13

Illustration of the origin of poleward component of the radiative force from a rotating star. *Left:* The poleward tilt of the radiative flux arising from the oblateness of the stellar surface contributes to a poleward component of the driving force. *Right:* Since the wind speed scales with surface escape speed, the lower effective gravity of the equator leads to a slower equatorial speed. The associated poleward increase in speed leads to a poleward tilt in the velocity gradient, and this again contributes to a poleward component of the line force

- Because lines have a thermally broadened velocity width ($v_{th} \lesssim a$) much less than the wind flow speed ($v \approx v_{esc}$), the absorption or scattering of photons in such an accelerating wind occurs over a narrow resonance layer (of width $l_{Sob} = v_{th}/(dv/dr) \approx (v_{th}/v_{esc})R$); following methods introduced by V. V. Sobolev, this allows nearly local solution of the line transfer in such accelerating flow.
- Within the CAK model for a power-law distribution of line strengths, the cumulative line-force scales with a power of the local velocity gradient divided by the density.
- For the idealized case of negligible gas pressure and a radially streaming point-source of stellar radiation, application of this CAK line-force within a steady-state radial equation of motion yields analytic scalings for the mass loss rate and wind velocity law.
- Accounting for the finite cone-angle of the stellar disk and radial ionization balance variations in the driving opacity yield order-unity corrections to the point-star scalings. Corrections for a finite gas pressure are smaller, of order 10%.
- Overall, the predictions of the CAK scalings agree well with an observationally inferred wind momentum–luminosity relation for OB supergiants.
- Careful analysis indicates that hot-star winds have extensive structure and variability, with small-scale turbulent structure likely arising from intrinsic instability of line-driving. The associated clumping has important implications for interpreting mass-loss rate diagnostics that scale with density squared.
- Rotation can also significantly affect the mass loss and wind speed, with the gravity darkening from rapid rotation leading to a somewhat surprising polar enhancement of wind density and flow speed.


6 Wolf-Rayet Winds and Multiline Scattering

The above CAK model is based on a simplified picture of absorption of the star's radiative momentum by many *independent* lines, effectively ignoring overlap effects among optically thick lines. Since each such thick line sweeps out a fraction v_∞/c of the star's radiative momentum L/c , the ratio of wind to radiative momentum is

$$\eta \equiv \frac{\dot{M}v_\infty}{L/c} = N_{thick} \frac{v_\infty}{c}, \quad (15.84)$$

which is sometimes termed the wind “momentum” or “performance” number. To avoid overlap, we must require $N_{thick} < c/v_\infty$, which in turn implies the so-called single-scattering limit for the wind momentum, $\eta < 1$. Since most OB winds are inferred to be below this limit, the basic CAK formalism ignoring overlap still provides a reasonably good model for explaining their overall properties.

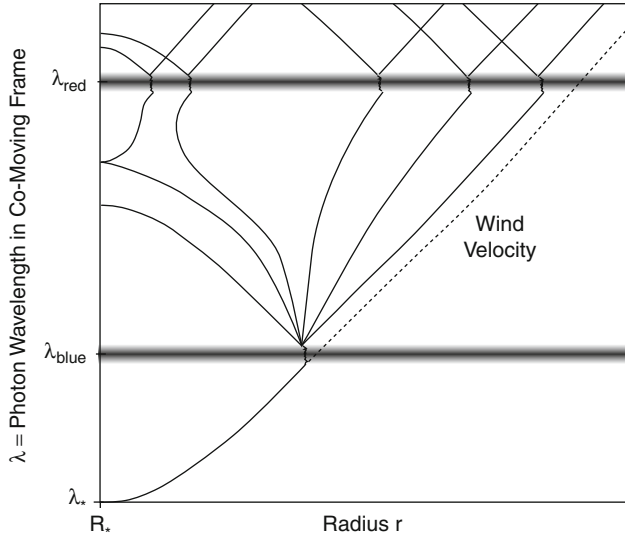
However, such a single-scattering formalism seems quite inadequate for the much stronger winds of Wolf-Rayet (WR) stars. Wolf-Rayet stars are evolved, massive, hot stars for which the cumulative mass loss has led to depletion of the original hydrogen envelope. They typically show broad wind-emission lines of elements like carbon, nitrogen, and/or oxygen that are the products of core nucleosynthesis. Overall, observations indicate that WR winds are especially strong, and even optically thick to continuum scattering by electrons. Notably, inferred WR wind momenta $\dot{M}v_\infty$ are generally substantially higher than for OB stars of comparable luminosity, placing them well above the OB-star line in the above wind momentum–luminosity relation. In fact, in WR winds the inferred momentum numbers are typically well above the single-scattering value $\eta = 1$, sometimes as high as $\eta = 10\text{--}50$!

This last property has often been cast as posing a WR wind “momentum problem,” sometimes with the implication that it means WR winds cannot be radiatively driven. In fact, it merely means that, unlike for OB stars, WR winds cannot be treated in the standard, single-scattering formalism. However, momentum ratios above unity can, in principle, be achieved by *multiple scattering* between overlapping thick lines with a velocity-unit frequency separation $\Delta\nu < v_\infty$.  *Figure 15-14* illustrates this for the simple case of two overlapping lines. But, as discussed below, the large momentum of WR winds requires much more extensive overlap, with thick lines spread densely throughout the spectrum without substantial gaps that can allow radiation to leak out. An overall theme here is that understanding WR mass loss represents more of an “opacity” than a “momentum” problem.

6.1 Example of Multiple Momentum Deposition in a Static Gray Envelope

To provide the basis for understanding such multiline scattering, it is helpful first to review the momentum deposition for *continuum* scattering. The total radial momentum imparted by radiation on a spherically symmetric circumstellar envelope can be expressed in terms of the radiative force density ρg_{rad} integrated over volume, outward from the wind base at radius R ,

$$\dot{p}_{rad} = \int_R^\infty 4\pi r^2 \rho g_{rad} dr, \quad (15.85)$$



■ Fig. 15-14

The Doppler-shifted line resonance in an accelerating flow, for two lines with relative wavelength separation $\Delta\lambda/\lambda < v_\infty/c$ close enough to allow multiline scattering within the wind. Photons scattered by the bluer line are reemitted with nearly equal probability in the forward or backward directions, but then further redshifted by the wind expansion into resonance with the redder line. Because of the gain in radial direction between the line resonances, the red-line scattering imparts an additional component of outward radial momentum

where the radiative acceleration is given by a frequency integral of the opacity κ_ν over the stellar flux spectrum, F_ν ,

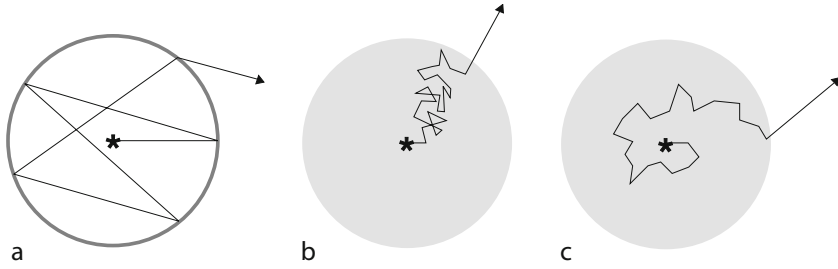
$$g_{rad} = \int_0^\infty \frac{\kappa_\nu F_\nu}{c} d\nu \tag{15.86}$$

A particularly simple way to illustrate the requirements of multiple momentum deposition is in terms of an envelope with a *gray* opacity κ . In this case, the flux is just a constant in frequency, set at each radius by the bolometric luminosity through $F = L/4\pi r^2$. This implies $g_{rad} = \kappa L/4\pi r^2 c$, and so yields

$$\dot{p}_{rad} = \frac{L}{c} \int_R^\infty \kappa \rho dr = \frac{L}{c} \tau, \tag{15.87}$$

where τ is the total wind optical depth. It is thus seen that the requirement for exceeding the single-scattering limit for radiative momentum deposition, $\dot{p}_{rad} > L/c$, is simply that the envelope be optically thick, $\tau > 1$.

► *Figure 15-15* provides a geometric illustration of how multiple momentum deposition occurs in an optically thick envelope. ► *Figure 15-15a* shows the case of a hollow shell with optical thickness $\tau = 5$, wherein a photon is backscattered within the hollow sphere roughly τ times before escaping, having thus cumulatively imparted τ times the single photon momentum, as given by (► 15.87).



■ Fig. 15-15

Schematic photon trajectories in (a) hollow and; (b) filled gray spheres, with part; (c) illustrating the net “winding” that makes even the filled case have a persistent net outward push that implies multiple radial momentum deposition (see text for details)

However, the same momentum deposition also occurs in a *solid* sphere with the same total optical depth, even though, as shown in ● Fig. 15-15b, photons in this case undergo a much more localized diffusion without hemispheric crossing.

● Figure 15-15c illustrates how these diffusive vs. direct-flight pictures of multiple momentum deposition can be reconciled by thinking in terms of an effective “winding” around the envelope. For each scattering within a spherical envelope, the radial momentum deposition is unchanged by arbitrary rotations about a radius through the scattering point. For ● Fig. 15-15c the rotations are chosen to bring all the scattered trajectories into a single plane, with the azimuthal component always of the same sense, here clockwise viewed from above the plane. In this artificial construction, scattering thus leads to a *systematic* (vs. random walk) drift of the photon along one azimuthal direction, implying a cumulative *winding* trajectory for which the systematic *outward* push of the scattered photon is now apparent.

6.2 Multiline Transfer in an Expanding Wind

The multiple scattering by a dense ensemble of lines can actually be related to the above gray envelope case, *if* the spectral distribution of lines is Poisson, and so is spread throughout the spectrum without extended bunches or gaps. As first noted by Friend and Castor (1983), and later expanded on by Gayley et al. (1995), a wind driven by such an effectively gray line-distribution can be analyzed through an extension of the above standard CAK formalism traditionally applied to the more moderate winds of OB stars. In the case of dense overlap, wherein optically thick lines in the wind have a frequency separation characterized by a velocity Δv much less than the wind terminal speed v_∞ , the mean-free-path between photon interactions with separate lines is given by

$$\frac{1}{\rho \kappa^{eff}} = \frac{\Delta v}{dv_n/dn}, \quad (15.88)$$

where $dv_n/dn \equiv \hat{\mathbf{n}} \cdot \nabla (\hat{\mathbf{n}} \cdot \mathbf{v})$ is the projected wind velocity gradient along a given photon direction $\hat{\mathbf{n}}$. The directional dependence of this velocity gradient implies an inherent *anisotropy* to the associated effectively gray line-ensemble opacity κ^{eff} . However, a full non-isotropic diffusion analysis (Gayley et al. 1995) indicates that the overall wind dynamics is not too sensitive to this anisotropy. In particular, the total wind momentum can still be characterized by the effective

radial optical depth, τ_r^{eff} , which in this case yields,

$$\dot{p}_{rad} \approx \frac{L}{c} \tau_r^{eff} = \frac{L}{c} \int_R^\infty \rho \kappa_r^{eff} dr = \frac{L}{c} \int_R^\infty \frac{1}{\Delta v} \frac{dv_r}{dr} dr = \frac{L}{c} \frac{v_\infty}{\Delta v}, \quad (15.89)$$

from which we identify $\tau_r^{eff} = v_\infty/\Delta v$. Neglecting a modest correction for gravitational escape, global momentum balance requires $\dot{p}_{rad} \approx \dot{M}v_\infty$, thus implying

$$\eta \approx \frac{v_\infty}{\Delta v}. \quad (15.90)$$

For winds driven by a gray ensemble of lines, it is thus seen that large momentum factors $\eta \gg 1$ simply require that there be a large number of optically thick lines overlapping within the wind, $v_\infty \gg \Delta v$.

Note that (► 15.90) implies that the mass loss scales as

$$\dot{M} \approx \frac{L}{c^2} \frac{c}{\Delta v}, \quad (15.91)$$

wherein it is noted that $c/\Delta v$ just represents the total, spectrum-integrated number of thick lines, N_{thick} . It is important to realize, however, that this number of thick lines is not fixed a priori, but is itself dependent on wind properties like the mass loss rate and velocity law.

Self-consistent solution is again possible though through an extension of the standard CAK formalism. The key is to account for the fact that radiation entering into resonance of each line does not in general come directly from the stellar core, but instead has been previously scattered by the next blueward overlapping line. In the limit of strong overlap, the transfer between lines can be treated as local diffusion, using however a non-isotropic diffusion coefficient to account for the directional variation of the velocity gradient. In analogy to the finite-disk correction for point-star CAK model, one can then derive a “non-isotropic diffusion” correction factor, f_{nid} , to account for the diffuse angle distribution of the previously line-scattered radiation as it enters into resonance with then next line. With this factor, one again finds that the mass loss follows a standard CAK scaling relation (► 15.73)

$$\dot{M} = f_{nid}^{1/\alpha} \dot{M}_{cak} = f_{nid}^{1/\alpha} \frac{L}{c^2} \frac{\alpha}{1-\alpha} \left[\frac{\bar{Q}\Gamma}{1-\Gamma} \right]^{(1-\alpha)/\alpha}. \quad (15.92)$$

where $f_{nid}^{1/\alpha}$ is typically about one half (see ► Fig. 15-6 of Gayley et al. 1995).

The wind velocity law in such multi-scattering models is found to have a somewhat more extended acceleration than in standard finite-disk CAK models, with velocity law indexes of roughly $\beta = 1.5-2$. The terminal speed again scales with the effective escape speed, $v_\infty \approx 3v_{esc}$.

This analysis shows that, within such “effectively gray” distribution of overlapping lines, multiline scattering can, in principle, yield momentum numbers $\eta \gg 1$ well in excess of the single-scattering limit. In this sense, there is thus no fundamental “momentum” problem for understanding WR winds.

6.3 Wind Momentum–Luminosity Relation for WR Stars

As noted above (► Sect. 5.2), this CAK mass-loss law together with the tendency for the terminal speed v_∞ to scale with the effective escape speed v_e implies the wind momentum–luminosity relation (► 15.75). For WR stars, such comparisons of wind momentum vs. luminosity show a

much greater scatter, but with momenta consistently above those inferred for OB stars, typically reflecting more than a factor 10 higher mass loss rate for the same luminosity (Hamann et al. 1995). If we assume the same $\alpha \approx 0.6$ that characterizes OB winds, (15.75) suggests that WR winds must have a line-opacity normalization \bar{Q} that is more than a factor $\approx 10^{\alpha/(1-\alpha)} \approx 30$ higher! Alternatively, this enhanced mass loss could also be obtained through a slightly lower α , representing a somewhat flatter number distribution in line opacity. For example, for stars with Eddington parameter $\Gamma \approx 1/2$ and O-star value for $\bar{Q} \approx 10^3$, simply decreasing from $\alpha = 0.6$ to $\alpha = 0.5$ yields the required factor $\bar{Q}^{1/0.5-1/0.6} \approx 10$ increase in \dot{M} .

While such a modest reduction in α may seem more plausible than a large increase in \bar{Q} , it is generally not clear what basic properties of WR winds could lead to either type of change in the line-opacity distribution. In this context, it thus seems useful here to distinguish the classical *momentum* problem of achieving the large inferred WR momentum numbers, from an *opacity* problem of understanding the underlying sources of the enhanced line opacity needed to drive the enhanced mass loss of WR winds. The wind momentum vs. luminosity relation given in (15.75) yields a scaling of wind momentum numbers with $\eta \sim L^{1/\alpha-1} \sim L^{2/3}$, implying that even OB winds should have large momentum numbers, even exceeding the single-scattering limit, for a sufficiently large luminosity. Viewed in this way, the fundamental distinguishing characteristic of WR winds is not so much their large momentum number, but rather their enhanced mass loss compared to OB stars with similar luminosity. Identifying the sources of the enhanced opacity required to drive this enhanced mass loss thus represents a fundamental, unsolved “opacity problem.”

6.4 Cumulative Comoving-Frame Redshift from Multiline Scattering

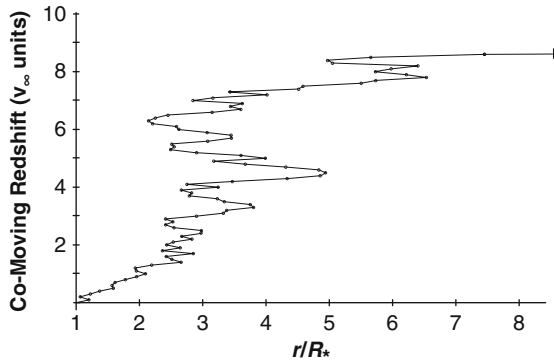
One can also view this multiline scattering that occurs in a WR wind as a random walk over wind *velocity*. To achieve the rms target velocity v_∞ in random increments of Δv requires stepping through $(v_\infty/\Delta v)^2$ lines. Since the expected net redshift from each line interaction is of order $\Delta v/c$, photons undergo a cumulative redshift $\Delta E/E \approx (v_\infty^2/\Delta v^2)\Delta v/c$ over the course of their escape. The associated radial momentum deposition factor is $\eta \approx (\Delta E/E)(c/v_\infty) \approx v_\infty/\Delta v$, as found above.

Figure 15-16 illustrates the comoving-frame redshift for a typical photon as it diffuses in radius due to multiline scattering. The photon track shown is a characteristic result of a simple Monte Carlo calculation for a wind velocity law $v(r) = v_\infty(1 - R/r)$ and a constant line spacing $\Delta v = v_\infty/10$. Each of the nodes shown represents scattering in one line. In this specific case, the photon escapes only after interacting with nearly 90 lines, resulting in cumulative redshift of nearly $9v_\infty/c$. These are near the statistically expected values of $(v_\infty/\Delta v)^2 = 100$ line scatterings resulting in a total redshift $v_\infty^2/c\Delta v = 10v_\infty/c$, as given by the above random walk arguments.

This systematic photon redshift can also be related to the energy loss – or photon “tiring” – that results from the *work* the radiation does to accelerate the wind to its terminal speed v_∞ . The ratio of wind kinetic energy to the radiative energy represents a “kinetic tiring number”

$$m_{kin} = \frac{\dot{M}v_\infty^2}{2L} = \eta \frac{v_\infty}{2c}. \quad (15.93)$$

Since typically $v_\infty/c < 0.01$, it is seen that for WR winds with momentum numbers of order $\eta \approx 10$, photon tiring is only a ~5% effect. Although thus not of much significance for either OB



■ Fig. 15-16

Simulated photon redshift in the comoving frame as a photon executes a random walk through the wind. The adopted line density is $v_\infty/\Delta v = 10$, which because of the random walk character, implies the photon will interact with roughly 10^2 different lines during escape. Since the comoving redshift between scatterings is $v_\infty/10$, this implies a total comoving redshift of $10 v_\infty$.

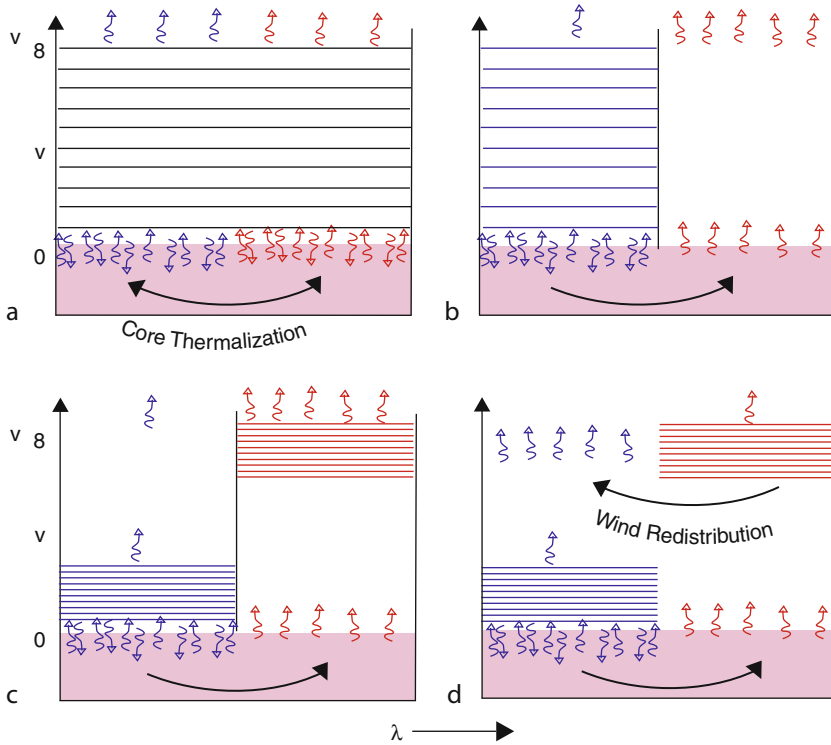
or WR winds, photon tiring does represent a fundamental limit to mass loss, with implications for understanding the giant eruptions from Luminous Blue Variable (LBV) stars.

6.5 Role of Line Bunches, Gaps, and Core Thermalization

An essential complication for developing realistic models of WR winds stems from the inherently non-Poisson character of the spectral-line distributions derived from atomic databases of line lists. At any given wind radius, the dominant contribution to the line opacity stems from a surprisingly small number of specific ionization stages of abundant heavy metals, primarily iron and iron-group elements. Moreover, for any given ion stage, the term “structure” is such that the lines are notably “bunched” into relatively restricted ranges of wavelength. With just a small number of distinct ion stages, the cumulative line spectrum thus likewise exhibits extensive wavelength bunching. Within the gaps between these bunches, the radiation can propagate relatively unimpeded by line scattering, thus representing a potential preferential “leakage” that can significantly reduce the global radiative momentum deposition.

To provide a physical perspective it is helpful to return to the above concept that the line-ensemble constitutes an effective *continuum* opacity, but now allowing this to be frequency dependent to account for the relative bunches and gaps in the spectral distribution of lines. As seen from (► 15.86), the radiative acceleration for such a non-gray opacity depends on the spectral integral of the opacity times the *frequency-dependent* radiation flux. In general, the flux spectrum at any given location in an atmosphere or wind depends on self-consistent solution of a global radiation transport problem, with overall characteristics depending critically on the *thermalization* and *frequency redistribution* properties of the medium.

► Figure 15-17a–d illustrate this key role of photon thermalization and redistribution for simple non-gray line-distributions that are divided locally into two distinct spectral regions, representing either a line “bunch” or “gap.” ► Figure 15-17a first recaps the effectively gray case



■ Fig. 15-17

Schematic diagram illustrating the role of line gaps, line bunches, and photon thermalization for WR wind momentum deposition. The horizontal lines represent the velocity/frequency spacing of optically thick lines in the wind. The four parts represent: (a) an effectively gray model; (b) a wind with fixed ionization and extensive gaps; (c) a wind with ionization stratification that fills gaps; (d) the importance of limiting energy redistribution in the wind

in which the entire spectrum is covered by lines at fixed velocity separation $\Delta v = v_\infty/10$. Since this represents a total effective optical depth $\tau = 10$ for photons to escape from the surface ($v = 0$) to infinity ($v = v_\infty$), the global radiative momentum is $\dot{p}_{rad} = 10L/c$, as follows from (► 15.87).

► Figure 15-17b represents the case when lines have the same concentration $\Delta v = v_\infty/10$ in half the spectrum (the bunch), with the other half completely line-free (the gap). Photons blocked in the bunched region are then rethermalized in the stellar core, and so tend to escape through the gap. Simple statistical arguments show that only about $0.5/(1 + \tau/2) = 1/12$ of the total flux now makes it out through the half of the spectrum covered by the bunch, implying from (► 15.87) that the total radiative momentum is now only $\dot{p}_{rad}/(L/c) \approx 10 \times 1/12 + 0 \times 11/12 = 5/6 < 1$! This roughly represents the circumstance applicable to OB star winds, which have radially constant ionization, and so a radially fixed line spectrum. For such winds, it can be seen that any significant spectral gaps keep the momentum number to near the single-scattering limit $\dot{p}_{rad} \approx L/c$, even if there is very extensive line overlap in spectral line bunches.

► *Figure 15-17c* represents the case wherein there are again $\tau = 10$ lines covering the full spectrum, but now over a limited spatial range, occurring very close to the star in one spectral region, and very far away in the other. In the region where line-blocking occurs near the star, core thermalization again channels photons to the other spectral region. But in this second spectral region, the blocking occurs far away from the star, with greatly reduced probability of backscattering to thermal redistribution in the stellar core. Again assuming purely coherent line scattering in the wind, this means the flux is nearly independent of the outer wind blocking. Since all the stellar flux must diffuse through a layer somewhere with $\tau = 10$ lines, the global momentum deposition is now again, as in case a, simply $\dot{p}_{rad} = 10L/c$. However, note that the flux distribution is still similar to case b, that is, in proportion 1/12 and 11/12 to the spectral regions corresponding respectively to the inner and outer wind blocking. This thus implies the same ratio for the relative deposition of radiative momentum. Overall it can be seen that this example, intended to represent the case of an optically thick WR wind with ionization stratification, does indeed illustrate how it is possible to get a large global momentum deposition even when the line-opacity spectrum is locally divided into gaps and bunches. However, this radiative momentum tends to be deposited more in the outer wind, leaving a net deficit in driving needed to initiate the outflow in the lower wind. This may play a factor in inducing the inferred structure and variability of WR winds.

The final example in ► *Fig. 15-17d* illustrates the crucial importance of the assumption that the radiative transfer within the wind itself is through pure, coherent scattering. If there is significant thermalization or any other type of spectral energy redistribution within the wind itself, then radiation will always tend to be channeled into local gaps, thus again limiting the momentum deposition to a level roughly characterized by the single-scattering limit.

6.6 Summary for Wolf–Rayet Winds

- The classical “momentum problem” (to explain the large inferred ratio of wind to radiative momentum, $\eta \equiv \dot{M}v_{\infty}/(L/c) \gg 1$) is in principle readily solved through multiple scattering of radiation by an opacity that is sufficiently “gray” in its spectral distribution. In this case, one simply obtains $\eta \approx \tau$, where τ is the wind optical depth.
- Lines with a Poisson spectral distribution yield an “effectively gray” cumulative opacity, with multilines scattering occurring when the velocity separation between thick lines Δv is less than the wind terminal speed v_{∞} . In this case, one obtains $\eta \approx v_{\infty}/\Delta v$.
- However, realistic line lists are not gray, and leakage through gaps in the line spectral distribution tends to limit the effective scattering to $\eta \lesssim 1$.
- In WR winds, ionization stratification helps spread line bunches and so fill in gaps, allowing for more effective global trapping of radiation, and thus $\eta > 1$.
- However, photon thermalization can reduce the local effectiveness of line-driving near the stellar core, making it difficult for radiation alone to initiate the wind.
- The relative complexity of WR wind initiation may be associated with the extensive turbulent structure inferred from observed variability in WR wind-emission lines.
- Overall, the understanding of WR winds is perhaps best viewed as an “opacity problem”, that is, identifying the enhanced opacity that can adequately block the radiation flux throughout the wind, and thus drive a WR mass loss that is much greater than from OB stars of comparable luminosity.

References

- Abbott, D. C. 1980, *ApJ*, 242, 1183
- Abbott, D. C. 1982, *ApJ*, 259, 282
- Allen, C. W. 1973, (3rd ed, London: University of London, Athlone Press)
- Biermann, L. 1951, Kometenschweife und solare Korpuskularstrahlung. *Zeitschrift für Astrophysik*, 29, 274
- Bjorkman, J. E., & Cassinelli, J. 1993, *ApJ*, 409, 429
- Breitschwerdt, D., & Komossa, S. 2000, Galactic fountains and galactic winds. *Ap&SS*, 272, 3–13
- Calvet, N. 2004, Outflows and accretion in young stellar objects, in *Stars as Suns : Activity, Evolution and Planets*, Proceedings of the 219th Symposium of the International Astronomical Union Held During the IAU General Assembly XXV, Sydney, ed. A. K. Dupree, & A. O. Benz (San Francisco, CA: ASP), 599
- Castor, J. I., Abbott, D. C., & Klein, R. 1975, *ApJ*, 195, 157
- Chamberlain, J. W. 1961, *ApJ*, 133, 675
- Chapman, S. 1961, *Space Astrophys*, 133, 675
- Cohen, D. H. 2008, *IAU Symposium*, 250, 17
- Cox, D. P., & Tucker, W. H. 1969, *ApJ*, 157, 1157
- Cranmer, S. R., et al. 1999, *ApJ*, 511, 481
- Cranmer, S. R. 2000, *ApJ*, 532, 1197
- Cranmer, S. R. 2009, Coronal holes. *Living Rev Solar Phys*, 6, 3. URL: <http://www.livingreviews.org/lrsp-2009-3>
- Cranmer, S. R., & Owocki, S. P. 1996, Hydrodynamical simulations of corotating interaction regions and discrete absorption components in rotating O-star winds. *ApJ*, 462, 469
- Cranmer, S. R., & Owocki, S. P. 1999, *ApJ*, 440, 308
- de Koter, A., Vink, J. S., & Muijres, L. 2008, in *Clumping in Hot-Star Winds*, 47, Proceedings of an International Workshop Held in Potsdam, ed. W. -R. Hamann, A. Feldmeier, L. M. Oskinova (Potsdam). ISBN 978-3-940793-33-1
- Dessart, L., & Owocki, S. P. 2003, Two-dimensional simulations of the line-driven instability in hot-star winds. *A&A*, 406, L1–L4
- Dessart, L., & Owocki, S. P. 2005, 2D simulations of the line-driven instability in hot-star winds. II. Approximations for the 2D radiation force. *A&A*, 437, 657–666
- Dupree, A. K. 2004, Winds from cool stars, in *Stars as Suns : Activity, Evolution and Planets*, Proceedings of the 219th Symposium of the International Astronomical Union Held During the IAU General Assembly XXV, Sydney, ed. A. K. Dupree, & A. O. Benz (San Francisco, CA: ASP), 623
- Feldmeier, A. 1995, *A&A*, 299, 523
- Friend, D. B., & Abbott, D. C. 1986, 311, 701
- Friend, D. B., & Castor, J. C. 1983, 272, 259
- Fullerton, A. W. 2003, Cyclical wind variability from O-type stars, in *Magnetic Fields in O, B and A Stars: Origin and Connection to Pulsation, Rotation and Mass Loss*, Proceedings of the Conference Held 27 November - 1 December, 2002 at University of North-West, Mmabatho, Vol. 305, ed. L. A. Balona, H. F. Henrichs, & R. Medupe (San Francisco: ASP), 333
- Fullerton, A. W., Massa, D. L., & Prinja, R. K. 2006, The discordance of mass-loss estimates for galactic O-type stars. *ApJ*, 637, 1025–1039
- Gayley, K. G. 1995, *ApJ*, 454, 410
- Gayley, K. G., Owocki, S. P., & Cranmer, S. R. 1995, *ApJ*, 442, 296
- Groenewegen, M. A. T., & Lamers, H. J. G. L. M. 1989, The winds of O-stars. I – an analysis of the UV line profiles with the SEI method. *A&AS*, 79, 359
- Groh, J. H., Madura, T. I., Owocki, S. P., Hillier, D. J., & Weigelt, G. 2010, Is Eta Carinae a fast rotator, and how much does the companion influence the inner wind structure? *ApJL*, 716, L223–L228
- Hamann, W.-R. 1996, Spectral analysis and model atmospheres of WR central stars (Invited paper). *Ap&SS*, 238, 31–42
- Hamann, W. R., Koesterke, L., & Wessolowski, U. 1995, *A&A*, 299, 151
- Hamann, W.-R., Gräfener, G., & Koesterke, L. 2003, WR central stars (invited review), in *Planetary Nebulae: Their Evolution and Role in the Universe*, Proceedings of the 209th Symposium of the International Astronomical Union held at Canberra, ed. S.Kwok, M. Dopita, & R. Sutherland (ASP)
- Hamann, W.-R., Feldmeier, A., & Oskinova, L. M. 2008, Clumping in hot-star winds, in *Clumping in Hot-Star Winds: Proceedings of an International Workshop Held in Potsdam*, ed. W. R. Hamann, A. Feldmeier, & L. M. Oskinova. ISBN 978-3-940793-33-1
- Hansen, C. J., Kawaler, S. D., & Trimble, V. 2004, *Stellar Interiors: Physical Principles, Structure, and Evolution* (2nd ed.; New York: Springer)
- Hartmann, L., & MacGregor, K. B. 1980, Momentum and energy deposition in late-type stellar atmospheres and winds. *ApJ*, 242, 260–282
- Howarth, I. D., & Prinja, R. K. 1989, The stellar winds of 203 Galactic O stars – A quantitative ultraviolet survey. *ApJS*, 69, 527–592
- Holzer, T. E., & MacGregor, K. B. 1985, Mass loss mechanisms for cool, low-gravity stars, in *IN: Mass Loss From Red Giants*; Proceedings of the

- Conference, Los Angeles (Dordrecht: D. Reidel Publishing Co.), 229–255
- Hillier, D. J. 2003, *Advances in modeling of Wolf-Rayet stars*, in *A Massive Star Odyssey: From Main Sequence to Supernova*, Proceedings of IAU Symposium #212, Held 24–28 June 2001 in Lanzarote, Canary island, ed. K. van der Hucht, A. Herrero, & C. Esteban (San Francisco: ASP), 70
- Hillier, D. J., & Miller, D. L. 1999, Constraints on the evolution of massive stars through spectral analysis. I. The WC5 star HD 165763. *ApJ*, 519, 354–371
- Holzer, T. E., Fla, T., & Leer, E. 1983, Alfvén waves in stellar winds. *ApJ*, 275, 808–835
- Holzer, T. E., & MacGregor, K. B. 1985, Mass Loss from Red Giants, 117, 229
- Holzer, T. E. 1987, Theory of winds from cool stars, in *IN: Circumstellar Matter; Proceedings of the IAU Symposium, Heidelberg* (Dordrecht: D. Reidel Publishing Co.), 289–305
- Kohl, J. L., Esser, R., Gardner, L. D., Habbal, S., Daigneau, P. S., Dennis, E. F., Nystrom, G. U., Panasyuk, A., Raymond, J. C., Smith, P. L., Strachan, L., van Ballegooijen, A. A., Noci, G., Fineschi, S., Romoli, M., Ciaravella, A., Modigliani, A., Huber, M. C. E., Antonucci, E., Benna, C., Giordano, S., Tondello, G., Nicolosi, P., Naletto, G., Pernechele, C., Spadaro, D., Poletto, G., Livi, S., von der Lühe, O., Geiss, J., Timothy, J. G., Gloeckler, G., Allegra, A., Basile, G., Brusa, R., Wood, B., Siegmund, O. H. W., Fowler, W., Fisher, R., & Jhabvala, M. 1995, The ultraviolet coronagraph spectrometer for the solar and heliospheric observatory. *Solar Phys*, 162, 313–356
- Kohl, J. L., Esser, R., Cranmer, S. R., Fineschi, S., Gardner, L. D., Panasyuk, A. V., Strachan, L., Suleman, R. M., Frazin, R. A., & Noci, G. 1999, *ApJ*, 510, L59
- Koninx, J. -P. M., & Pijpers, F. P. 1992, The applicability of the linearized theory of sound-wave driven winds. *A&A*, 265, 183–194
- Kudritzki, R. P., Lennon, D. J., & Puls, J. 1995, Quantitative Spectroscopy of luminous blue stars in distant galaxies. in *Science with the VLT*, eds. J. R. Walsh & I. J. Danziger (Berlin: Springer), 246
- Lamers, H. J. G. L. M., & Cassinelli, J. 1999, *Introduction to Stellar Winds* (Cambridge/New York: Cambridge University Press)
- Lamers, H. J. G. L. M., Cerruti-Sola, M., & Perinotto, M. 1987, The ‘SEI’ method for accurate and efficient calculations of line profiles in spherically symmetric stellar winds. *ApJ*, 314, 726–738
- Leer, E., & Holzer, T. E. 1979, *Solar Phys.*, 63, 143
- Leer, E., Holzer, T. E., & Fla, T. 1982, Acceleration of the solar wind. *SSRv*, 33, 161–200
- Lépine, S., & Moffat, A. F. J. 1999, *ApJ*, 514, 909
- Li, A., in “The Spectral Energy Distribution of Gas-Rich Galaxies: Confronting Models with Data”, edited by C.C. Popescu & R.J. Tuffs, *AIP Conf. Proc.* 761, pp. 123–133
- Lucy, L. B. 1982, *ApJ*, 255, 278
- Lucy, L. B. 1984, 284, 351
- MacGregor, K. B., Hartmann, L., & Raymond, J. C. 1979, *ApJ*, 231, 514
- Maeder, A., & Meynet, G. 2000, *ARA&A*, 38, 143
- Maksimovic, M., Issautier, K., Meyer-Vernet, N., Moncuquet, M., & Pantellini, F. 2010, in *Twelfth International Solar Wind Conference. AIP Conference Proceedings*, Vol. 1216
- McComas, D. J., Bame, S. J., Barraclough, B. L., Feldman, W. C., Funsten, H. O., Gosling, J. T., Riley, P., Skoug, R., Balogh, A., Forsyth, R., et al. 1998, Ulysses’ return to the slow solar wind. *GeoRL*, 25, 1–4
- Meyer-Vernet, N. 2007, *Basics of the Solar Wind* (Cambridge, UK: Cambridge University Press). ISBN-10 0-521-81420-0 (HB); ISBN-13 978-0-521-81420-1 (HB)
- Mihalas, D. 1978, (San Francisco: W. H. Freeman and Co.), 650
- Mihalas, D. 1978, *Stellar Atmospheres* (San Francisco: Freeman)
- Mullan, D. J. 1984, Corotating interaction regions in stellar winds. *ApJ*, 283, 303–312
- Newkirk, G. 1967, Structure of the solar corona. *Ann Rev Astron Astrophys*, 5, 213–266
- Oey, M. S., & Clarke, C. J. 2007, Massive stars: feedback effects in the local universe. eprint arXiv:astro-ph/0703036
- Owocki, S. P. 1999, Co-rotating interaction regions in 2D hot-star wind models with line-driven instability, in *IAU Colloq. 169: Variable and Non-spherical Stellar Winds in Luminous Hot Stars. Lecture Notes in Physics*, Vol 523, ed. B. Wolf, O. Stahl, & A. W. Fullerton (Berlin: Springer), 294
- Owocki, S. 2001, Radiatively driven stellar winds from hot stars, in *Encyclopedia of Astronomy and Astrophysics*, ed. P. Murdin, article 1887 (Bristol: Institute of Physics Publishing)
- Owocki, S. 2004, Stellar wind mechanisms and instabilities, in *Evolution of Massive Stars, Mass Loss and Winds*, Held in Aussois and Oléron. *EAS Publications Series*, Vol. 13. doi:10.1051/eas:2004055
- Owocki, S. P., & Puls, J. 1996, Nonlocal escape-integral approximations for the line force

- in structured line-driven stellar winds. *ApJ*, 462, 894
- Owocki, S. P., & Puls, J. 1999, Line-driven stellar winds: the dynamical role of diffuse radiation gradients and limitations to the Sobolev approach. *ApJ*, 510, 355–368
- Owocki, S. P., & ud-Doula, A. 2004, The effect of magnetic field tilt and divergence on the mass flux and flow speed in a line-driven stellar wind. *ApJ*, 600, 1004–1015
- Owocki, S. P., Castor, J. I., & Rybicki, G. B. 1988, *ApJ*, 335, 914
- Owocki, S. P., Cranmer, S. R., & Blondin, J. 1994, *ApJ*, 424, 887
- Owocki, S. P., Cranmer, S. R., & Gayley, K. G. 1996, *ApJ*, 472, L115
- Owocki, S. P., Gayley, K. G., & Shaviv, N. J. 2004, A porosity-length formalism for photon-tiring-limited mass loss from stars above the Eddington limit. *ApJ*, 616, 525–541
- Owocki, S. P., & Rybicki, G. B. 1984, *ApJ*, 284, 337
- Owocki, S. P., & Rybicki, G. B. 1985, *ApJ*, 299, 265
- Parker E. N. 1963, *Interplanetary Dynamical Processes* (New York: Interscience Publishers)
- Pauldrach, A. W. A., Puls, J., & Kudritzki, R. P. 1986, *A&A*, 164, 86
- Proga, D. 2007, Theory of winds in AGNs, in *The Central Engine of Active Galactic Nuclei*, ASP Conference Series, Vol. 373, Proceedings of the Conference Held 16-21 October, 2006 at Xi'an Jiaotong University, Xi'an, ed. L. C. Ho, & J. -M. Wang (ASP), 267
- Puls, J., Kudritzki, R. P., Herrero, A., Pauldrach, A. W. A., Haser, S. M., Lennon, D. J., Gabler, R., Voels, S., Vilchez, J. M., & Feldmeier, A. 1996, *A&A*, 305, 171
- Puls, J., Markova, N., Scuderi, S., Stanghellini, C., Taranova, O. G., Burnley, A. W. & Howarth, I. D. 2006, Bright OB stars in the Galaxy. III. Constraints on the radial stratification of the clumping factor in hot star winds from a combined H α , IR and radio analysis. *A&A*, 454, 625–651
- Puls, J., Vink, J. S., & Najarro, F. 2008, Mass loss from hot massive stars. *A&ARv*, 16, 209–325
- Raymond, J. C., Cox, D. P., & Smith, B. W. 1976, *ApJ*, 204, 290
- Scholz, A. 2009, Stellar spindown: from the ONC to the sun, in *Cool Stars, Stellar Systems And The Sun: Proceedings of the 15th Cambridge Workshop on Cool Stars, Stellar Systems and the Sun*. AIP Conference Proceedings, Vol. 1094. doi:10.1063/1.3099189
- Smith, N., Davidson, K., Gull, T. R., Ishibashi, K., Hillier, D. J. 2003, *ApJ*, 586, 432
- Sobolev, V. V. 1960, *Moving Envelopes of Stars* (Cambridge, MA: Harvard Univ. Press)
- Spitzer, L. 1962, *Physics of Fully Ionized Gases* (2nd ed; New York: Interscience)
- Townsend, R. H. D., Owocki, S. P., & Howarth, I. D. 2004, Be-star rotation: how close to critical? *MNRAS*, 350, 189–195
- Van Loo, S. 2005, Non-thermal radio emission from single hot stars. PhD thesis, Katholieke Universiteit Leuven
- van Boekel, R., Kervella, P., Schoeller, M., Herbst, T., Brandner, W., de Koter, A., Waters, L., Hillier, D. J., Paresce, F., Lenzen, R., & Lagrange, A. -M. 2003, *A&A*, 410, L37
- von Zeipel, H. 1924, *MNRAS*, 84, 665
- Vink, J. S. 2008, Mass loss and evolution of hot massive stars, in *The Art of Modeling Stars in the 21st Century*, Proceedings of the International Astronomical Union. IAU Symposium, Vol. 252, 271–281. doi:10.1017/S1743921308023016
- Weber, E. J., & Davis, L., Jr. 1967, The angular momentum of the solar wind. *ApJ*, 148, 217–227
- Willson, L. A. 2000, Mass loss from cool stars: impact on the evolution of stars and stellar populations. *ARA&A*, 38, 573–611
- Willson, L. A. 2008, Deathzones and exponents: a different approach to incorporating mass loss in stellar evolution calculations, in *The Art of Modeling Stars in the 21st Century*, Proceedings of the International Astronomical Union. IAU Symposium, Vol. 252, 189–195. doi:10.1017/S1743921308022758
- Withbroe, G. L. 1988, The temperature structure, mass, and energy flow in the corona and inner solar wind. *ApJ*, 325, 442–467
- Withbroe, G. L. 1989, The solar wind mass flux. *ApJ*, 337, L49–L52
- Wood, B.E., 2004, Astrospheres and solar-like stellar winds. *Living Rev Solar Phys*, 1, Irsp-2004-2
- Wright, A. E., & Barlow, M. J. 1975, The radio and infrared spectrum of early-type stars undergoing mass loss. *MNRAS*, 170, 41–51
- Zirker, J. 1977, *Coronal Holes & High-speed Wind Streams* (Boulder : Colorado Associated University Press)